

University of Alberta

**OXIDATION SYNTHESIS AND
REACTION ANALYSIS OF A NEW
ARRANGED CATALYST SUPPORT**

by

Jadid Ettaz Samad

A thesis submitted to the Faculty of Graduate Studies and Research
in partial fulfillment of the requirements for the degree of

Master of Science in Chemical Engineering

Department of Chemical and Materials Engineering

© Jadid Ettaz Samad

Fall 2010

Edmonton, Alberta

Permission is hereby granted to the University of Alberta Libraries to reproduce single copies of this thesis and to lend or sell such copies for private, scholarly or scientific research purposes only. Where the thesis is converted to, or otherwise made available in digital form, the University of Alberta will advise potential users of the thesis of these terms.

The author reserves all other publication and other rights in association with the copyright in the thesis and, except as herein before provided, neither the thesis nor any substantial portion thereof may be printed or otherwise reproduced in any material form whatsoever without the author's prior written permission.

Examining Committee

Dr. John A. Nychka, Chemical and Materials Engineering (Supervisor)

Dr. Natalia Semagina, Chemical and Materials Engineering (Co-Supervisor)

Dr. Weixing Chen, Chemical and Materials Engineering

Dr. André G. McDonald, Mechanical Engineering

Dedicated

To my parents

I understand they wanted me to become a doctor. But they never spoke a single word about it. They let me choose my own path.

Abstract

In this study, a new arranged catalyst support with distinct open pore morphology has been fabricated via thermal oxidation of an FeCrAl alloy with an aim to address mass transfer limitations that conventional supports have due to their internal porosity. Subsequent characterization tests including, drop shape analysis, X-ray diffraction, X-ray photoelectron spectroscopy and scanning electron microscopy revealed that the support formed upon thermal oxidation for 1 hour at 930°C, 1 hour at 960°C and 2 hours at 990°C embodies advantageous support characteristics. Preliminary tests were performed using palladium (active component) deposited on the new support in representative three phase hydrogenation reactions of 2-methyl-3-butyn-2-ol or 2-methyl-3-buten-2-ol. Absence of mass transfer limitations was verified for 2-methyl-3-buten-2-ol hydrogenation at 35-50°C, 1200 rpm stirring speed and 0.46 MPa pressure of hydrogen in a 300 ml semi-batch reactor using ethanol as solvent. The study paves the way to the development of arranged catalysts based on FeCrAl alloy fibers for structured reactors.

Acknowledgements

I would like to begin by expressing my heartfelt gratitude and appreciation to Prof. John A. Nychka and Prof. Natalia Semagina who instilled in me a spirit of adventure and excitement in regard to scientific research. Through their excellent mentorship and patience they have transformed a graduate student who began with only a handful of motivation to someone who now carries the belief, desire and skill, in short, the ingredients of success. Without them this dissertation and all the interdisciplinary work related to it would not have been possible. It was such a great honor for me to be guided by them.

I would also like to thank my honorable committee members, Dr. Weixing Chen and Dr. André G. McDonald for agreeing to review my work and Dr. Anthony Yeung for being the oral exam chair.

Many others, directly or indirectly, have contributed to the accomplishment of this work. I would like to acknowledge the Natural Sciences and Engineering Research Council of Canada for financial support of this research through the Strategic Projects Grant program. Also thanks to John Adjaye of Syncrude Canada Ltd., Edmonton Research Center for his in-kind support and feedback. I am also grateful to Alberta Center for Surface Engineering and Science (ACSES) for providing assistance with SEM and XPS analysis, Professor Zhenghe Xu (University of Alberta) for use of his DSA apparatus, Shiraz Merali (University of Alberta) for assistance with XRD, Arlene Oatway (Biological Sciences microscopy unity, University of Alberta) for SEM and Katie Krause (PhD student, Department of Electrical and Computer Engineering, University of Alberta) for doing BET surface area measurements at National Institute of Nanotechnology (NINT), University of Alberta. Finally, thanks to the members of my research group, Hamidreza Pirayesh and Satadru Kashyap for their help to develop my knowledge in Materials engineering and Ran Ma for her invaluable feedback and help during reaction runs.

Table of contents

CHAPTER 1	1
INTRODUCTION	1
CHAPTER 2	4
IMPORTANT FEATURES OF THREE PHASE HYDROGENATIONS	4
2.1 THREE PHASE HYDROGENATION	4
2.2 HETEROGENEOUS CATALYSTS	4
2.2.1 <i>Catalyst support</i>	5
2.2.2 <i>Integrating active components with support</i>	5
2.2.3 <i>Effects of particle size and support texture</i>	8
2.3 ACTION SEQUENCE IN THREE PHASE HYDROGENATION REACTION	9
2.3.1 <i>External mass transfer (film diffusion)</i>	10
2.3.2 <i>Internal Mass Transfer</i>	12
2.4 CATALYST DEACTIVATION	13
2.4.1 <i>Poisoning</i>	13
2.4.2 <i>Deposition of coke and/or inactive metals</i>	13
2.4.3 <i>Sintering and leaching of active components</i>	14
2.4.4 <i>Mechanical failure</i>	14
2.5 APPLICATIONS OF HYDROGENATION REACTION	15
2.5.1 <i>Food industry</i>	15
2.5.2 <i>Petroleum industry</i>	15
CHAPTER 3	17
STRUCTURED REACTORS	17
3.1 MONOLITHIC CATALYSTS	17
3.1.1 <i>Main features</i>	18
3.1.2 <i>Monoliths in multiphase reactions</i>	19
3.1.3 <i>Two phase flow patterns in capillary monoliths</i>	20
3.2 MEMBRANE CATALYSTS	20
3.2.1 <i>Membrane reactors in multiphase systems</i>	21
3.3 ARRANGED CATALYSTS	22
3.4 MICROSTRUCTURED REACTORS	23

CHAPTER 4	25
ALUMINA CATALYST SUPPORTS:NATURE AND FABRICATION	25
4.1 DIFFERENT POLYTYPES OF ALUMINA.....	25
4.2 USE OF ALUMINA AS A SUPPORT.....	25
4.3 PREPARATION OF ALUMINA SUPPORT	26
4.3.1 Alumina formed via thermal oxidation	26
4.4 EFFECTS OF REACTIVE ELEMENTS ON THE OXIDATION PROCESS.....	27
4.5 WETTABILITY OF ALUMINA	28
4.5.1 Influence of roughness on wettability	28
CHAPTER 5	30
EXPERIMENTAL METHODS	30
5.1 MATERIALS.....	30
5.1.1 FeCrAl alloy.....	30
5.1.2 2-methyl-3-butyn-2-ol (MBY).....	31
5.1.3 2-methyl-3-buten-2-ol (MBE).....	31
5.1.4 Hydrogen.....	32
5.1.5 Nitrogen.....	32
5.1.6 Ethanol (solvent)	32
5.1.7 Pd precursor.....	32
5.1.8 Water	32
5.2 OXIDATION	32
5.2.1 FeCrAl coupons (Kanthal Al)	33
5.2.2 SMF.....	34
5.3 DEPOSITION OF Pd	35
5.4 CATALYTIC HYDROGENATION	36
5.4.1 Experimental setup.....	36
5.4.2 Determination of reactants and products concentration	36
5.5 CHARACTERIZATION OF SUPPORT CATALYSTS.....	37
5.5.1 Drop Shape Analysis (DSA)	37
5.5.2 X-Ray Diffraction (XRD).....	38
5.5.3 X-Ray Photoelectron Spectroscopy (XPS)	38
5.5.4 Scanning Electron Microscopy (SEM).....	38
5.5.5 Atomic Absorption Spectroscopy (AAS).....	38
5.5.6 Brunauer–Emmett–Teller (BET) surface area.....	39

CHAPTER 6	40
RESULTS AND DISCUSSION.....	40
6.1 DEVELOPMENT AND CHARACTERIZATION OF NEW SUPPORT.....	40
6.1.1 <i>Single stage oxidation</i>	40
6.1.2 <i>Multiple stage temperature oxidation</i>	47
6.1.3 <i>Oxidation of sintered metal fiber (SMF)</i>	50
6.2 THREE PHASE HYDROGENATION REACTION.....	56
6.2.1 <i>MBE hydrogenation</i>	58
6.2.2 <i>MBY hydrogenation</i>	61
CHAPTER 7	66
CONCLUSIONS.....	66
CHAPTER 8	68
FUTURE WORK.....	68

List of Tables

Table 1-1. Experimental schemes of this project	3
Table 5-1. Product specifications of FeCrAl strip [82] and SMF	30
Table 6-1. Observed contact angles for FeCrAl samples oxidized for different times. ...	41
Table 6-2. Multiple stage oxidation schemes	47
Table 6-3. Results obtained from the calculation of Carberry number	65

List of Figures

Figure 1.1. Schematics of (a) conventional and (b) proposed catalyst supports for three phase hydrogenation reactions.	1
Figure 2.1. Steps of three phase hydrogenation reaction.	10
Figure 3.1. Schematic of Taylor flow in Monolithic reactor for three phase hydrogenation system.	19
Figure 3.2. Schematic illustration and photograph of string reactor [55] [reused with permission from <i>Chemical Engineering Journal</i>].....	24
Figure 4.1. Different wettability modes: (a) Wenzel and (b) Cassie-Baxter.	28
Figure 5.1. Photographic image of (a) FeCrAl strip and (b) Sintered metal fiber (SMF). Scale bar is 3 mm.	31
Figure 5.2. Schematic drawing of the semibatch reactor setup for three phase hydrogenation reaction using sintered metal fiber (SMF) as catalyst. This illustration is not drawn to scale.	37
Figure 6.1. Relationship between oxidation time (t_{ox}) and contact angle (Θ) on oxidized alloy surface. XRD information on different alumina polytypes found to be present at different t_{ox} has been superimposed along the top axis. The baseline contact angle range for the unoxidized polished metal surface and compact alumina oxide scale (thermal oxidation at 1200°C for $t_{ox} = 25$ hrs) fell within the gray band around $\Theta = 50^\circ$	42
Figure 6.2. Image of ~8ml water drops on: (a) unoxidized FeCrAl alloy ($\Theta = 46.7^\circ$), (b) oxidized at 930°C for $t_{ox} = 0.25$ hr ($\Theta = 30.4^\circ$), (c) oxidized at 930°C for $t_{ox} = 24$ hrs ($\Theta = 128^\circ$), (d) oxidized at 1200°C for $t_{ox} = 25$ hrs ($\Theta = 33.4^\circ$).	42
Figure 6.3. XRD profile for different oxidation times: (a) $t_{ox} = 0.25$ hr, (b) $t_{ox} = 1$ hr, (c) $t_{ox} = 5$ hrs, (d) $t_{ox} = 10$ hrs, (e) $t_{ox} = 24$ hrs, (f) $t_{ox} = 48$ hrs, (g) $t_{ox} = 96$ hrs. Here α is shown as the representative of Rhombohedral alumina, γ of cubic alumina and θ of monoclinic alumina.	44
Figure 6.4. XPS plots of oxidized alloy surfaces with (a) C1s, and (b) O1s. (a) reveals that there is no distinct tendency for C contamination, and (b) reveals the absence of hydroxyl group in all specimens	44
Figure 6.5. SEM images of oxidized FeCrAl surfaces for variable lengths of time. Corresponding sessile water drop image (top right) and t_{ox} values (bottom left)	

attached with each image. Horizontal marker bar applicable for all images showed on the top left corner.....	45
Figure 6.6. (a) Schematic of platelet width, w , interplatelet distance, d , and thickness, r , measurements, and relationship between: (b) platelet width and t_{ox} , (c) interplatelet distance, thickness and t_{ox} . Note: all measurements were taken from plan view SEM micrographs.....	48
Figure 6.7. Measurement of scale height (h_{ox}) from etched edge of oxidized FeCrAl with (a) showing a representative cross-section; a layer of oxide scale on base metal (Oxidation condition: $T = 930^{\circ}\text{C}$ and $t_{ox} = 24$ hrs) and (b) showing evidence of bilayer oxide formation (Oxidation condition: $T = 930^{\circ}\text{C}$ and $t_{ox} = 2$ hrs) where, $h_{ox} = h_c + h_p$	49
Figure 6.8. Observed correlation between: (a) scale height and t_{ox} (Inset: Equation and related parameters obtained via curve fitting) and (b) platelet height, h_{op} (taken as $1/3^{\text{rd}}$ of the overall scale height, h_{ox}) and contact angle.	49
Figure 6.9. SEM micrographs of multiple stage oxidation. Inset: Operating conditions. All images have been taken at 30° tilt except the one oxidized for 1 hr at 960°C and 1 hr @ 1005°C which was taken at 0° tilt. Scale bar attached with the top left image is applicable for all images.....	50
Figure 6.10. SMFs oxidized at different multiple stage temperatures. Scale bar is $20\ \mu\text{m}$. Operating condition has been attached with each image.	51
Figure 6.11. (a) Higher resolution image of catalyst support (oxidation condition: 1 hr at 930°C , 1 hr at 960°C and 2 hrs at 990°C). (b) Simple schematic of whiskers formed at (a).....	52
Figure 6.12. XRD profile of SMF oxidized at multiple stage (Oxidation condition: 1 hr at 930°C , 1 hr at 960°C and 2 hrs at 990°C)......	53
Figure 6.13. DSA images water drops and contact angle values of oxidized and unoxidized SMF.	54
Figure 6.14. High resolution XPS spectrum of Pd 3d. Inset: different forms of Pd and their atomic percentages (Cl was found in survey plot with composition of $\sim 1.7\text{wt}\%$ compared to $\sim 4.6\text{wt}\%$ Pd).	54
Figure 6.15. SEM microphotographs of (a) bare SMF, (b) oxidized SMF and (c) oxidized SMF after Pd deposition.....	55
Figure 6.16. Mass loss profile upon immersion in acid for both oxidized and unoxidized specimens.	56

Figure 6.17. Three phase hydrogenation reaction schemes. Red arrow indicates reaction path for scheme 1 and black arrow (path a,b,c) indicates reaction paths for scheme 2.	57
Figure 6.18. Change in reaction rate with stirring speed. Reaction conditions: 50°C, 0.46 MPa H ₂ , 0.12 mg Pd (calculated from AAS).	58
Figure 6.19. Arrhenius plot constructed for the temperature range of 35° - 50°C. Reaction conditions: 0.46 MPa H ₂ , 0.14 mg ± 0.04 Pd (calculated mass from AAS).	60
Figure 6.20. Kinetics curves of MBY hydrogenation. Reaction conditions: 40°C, 1200 rpm stirring speed, 0.46 MPa H ₂ pressure, 0.09 mg Pd (calculated mass from AAS).	62
Figure 6.21. Selectivity to MBE vs. MBY conversion	63

List of symbols

Symbol	Description	Unit
$C_{H_2}^*$	Saturation concentration of hydrogen	$[\text{mol.m}^{-3}]$
P_{H_2}	Partial pressure of hydrogen	[Pa]
H_{H_2}	Henry's coefficient of hydrogen	$[\text{m}^3.\text{mol}^{-1}.\text{Pa}]$
m_{gl,H_2}	Mass transfer rate (gas-liquid)	$[\text{mol.m}^{-3}.\text{s}^{-1}]$
m_{ls}	Mass transfer rate (liquid-solid)	$[\text{mol.m}^{-3}.\text{s}^{-1}]$
k_l	Mass transfer coefficient (gas-liquid)	$[\text{m.s}^{-1}]$
k_s	Mass transfer coefficient (liquid-solid)	$[\text{m.s}^{-1}]$
a_l	Volumetric surface area (gas-liquid)	$[\text{m}^{-1}]$
a_s	Volumetric external surface area of the catalyst	$[\text{m}^{-1}]$ or $[\text{m}^2/\text{kg}]$
C_l	Concentration in liquid	$[\text{mol.m}^{-3}]$
$C_{H_2,liq}$	Concentration of hydrogen in liquid	$[\text{mol.m}^{-3}]$
R	Reaction rate	$[\text{mol.kgcat}^{-1}.\text{s}^{-1}]$
L_p	Pore length	[m]
D_{eff}	Effective diffusion coefficient inside the pores	$[\text{m}^2.\text{s}^{-1}]$
D	Diffusion coefficient in the liquid	$[\text{m}^2.\text{s}^{-1}]$
τ	Tortuosity factor	-
ε	Porosity	-
x_i	Mass concentration	-
C_i	Molar concentration	-
Θ	Contact angle	$[\text{°}]$
t_{ox}	Oxidation time	[min] or [hr]
T	Temperature	$[\text{°C}]$
h_{ox}	Oxide scale height	$[\mu\text{m}]$
h_p	Platelet height	$[\mu\text{m}]$
h_c	Compact layer height	$[\mu\text{m}]$
r	Platelet thickness	[nm]
d	Interplatelet distance	[nm]
W	Platelet width	[nm]
ρ_s	Density of support	$[\text{kg/m}^3]$
χ	Solvent association factor	-
η	Viscosity of ethanol	$[\text{Pa.s}]$
V	Molar volume of H_2	m^3/mol
Sc	Schmidt number	-
Sh	Sherwood number	-
N	Power number	-
l	Impeller diameter	[m]
n	Angular velocity	$[\text{rad/s}]$
ρ	Density of ethanol	$[\text{kg/m}^3]$
V_L	Liquid volume	$[\text{m}^3]$
d_p	Catalyst particle diameter	[m]

Ca	Carberry number	-
WW	Wheeler-Weisz group	-

List of abbreviations

Acronyms	Elaboration
SMF	Sintered metal fiber
MBE	2-methyl-3-buten-2-ol
MBY	2-methyl-3-butyn-2-ol
MBA	2-methylbutan-2-ol
IEP	Isoelectric point
DSA	Drop shape analysis
XPS	X-ray photoelectron spectroscopy
XRD	X-ray diffraction
SEM	Scanning electron microscopy
AAS	Atomic absorption spectroscopy
BET	Brunauer-Emmett-Teller (Surface area analysis)

Chapter 1

Introduction

Catalytic hydrogenations are part and parcel of heavy oil upgrading processes. Dwindling oil resources and soaring oil price are forcing people to exploit the heavier oil fractions that were regarded as ‘waste’ not so long ago. Alberta has vast proven reserves of heavy oil in the form of oil sands in which heavy metal and other impurity (S, N) contents are higher as compared to other oils. This heavy oil or oil sands upgrading via catalytic hydrogenation is currently achieved at a heavy price primarily due to the occurrence of rapid catalyst deactivation and inefficient use of catalytic surface by the reactants.

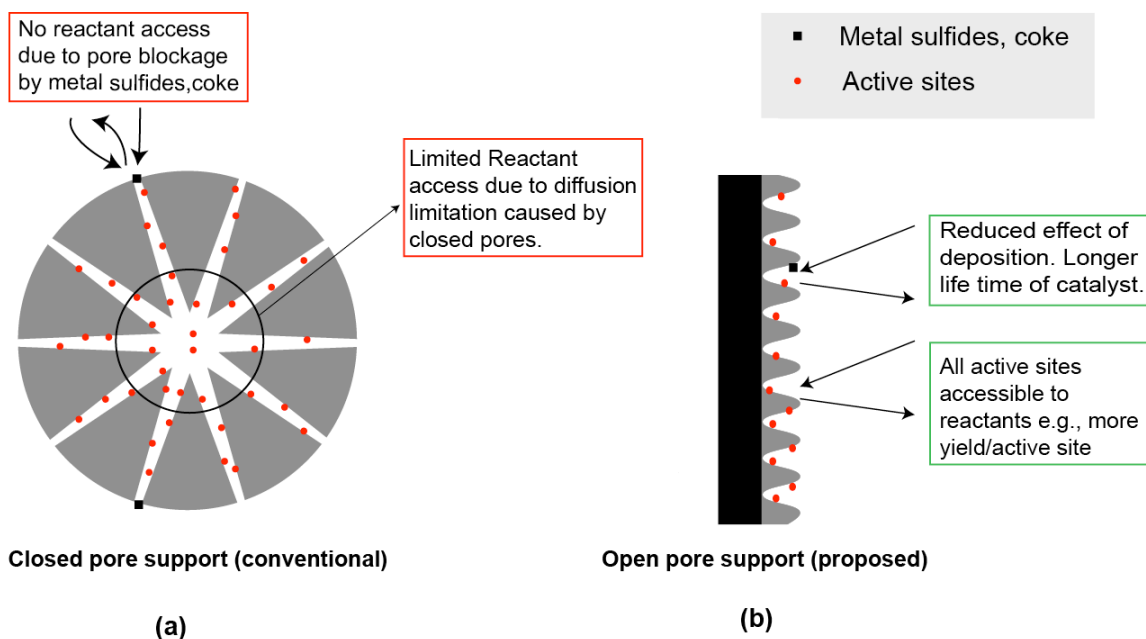


Figure 1.1. Schematics of (a) conventional and (b) proposed catalyst supports for three phase hydrogenation reactions.

The functioning of conventional catalyst supports depends on their porous structures. However, significant diffusion limitation, starting from the mouth of these pores, precludes reactants to reach further inside the pores. As a result, a considerable part (mainly near the core) of the high surface area of these porous structures becomes unusable. Another underlying disadvantage of porous structures is that during upgrading

process when heavy metal sulfides and coke form, they clog the pores. This often results in loss of catalytic efficiency as the catalyst very soon becomes spent and needs to be regenerated (Figure 1.1a).

Inversion of the porous structures could be one realistic solution to address this problem persisting with the conventional catalysts. One simple way to fabricate such structures would be thermal oxidation of some commercial metal alloys. Bearing this in mind, the following objectives have been chalked out for this project:

- 1) Fabrication of catalytic support via simple *in situ* thermal oxidation of a commercial alloy.
- 2) Identification of the most suitable support and its underlying processing technique (time, temperature) from different characterization tests.
- 3) Testing the mechanical and chemical stability of the selected support.
- 4) Deposition of catalytically active metal, Pd on the support.
- 5) Examination of mass transfer limitations in representative three phase hydrogenation reactions of functionalized alkyne and alkene.

For objective 1, two different oxidation schemes have been studied on a commercial corrosion resistant alumina forming alloy, FeCrAl: (a) at isothermal conditions and (b) at multiple stage temperature conditions. Resulting oxidized surfaces were characterized using Drop Shape Analysis (DSA), X-Ray Diffraction (XRD), X-ray Photoelectron Spectroscopy (XPS) and Scanning Electron Microscopy (SEM) in order to accomplish objective 2. However, change in wettability of the oxide surfaces was extensively studied due to its multifarious application potentials. Mechanical stability (outlined in objective 3) of the oxide support was tested using ultrasonic treatment whereas chemical stability was examined by immersion in a strong acid. Pd was used as active sites and was deposited by incipient wetness impregnation technique. Objective 5 was accomplished by estimating Carberry number, Wheeler-Weisz criterion, activation energy and stirring rate effects. Hydrogenations of unsaturated hydrocarbons 2-methyl-3-butyl-2-ol (MBY) and 2-methyl-3-buten-2-ol (MBE) were the two reactions studied in this project. Along with

the kinetic curve for the overall process, selectivity was also determined. MBE represents a model compound found in oil (C=C bonds) while MBY hydrogenation allows analyzing catalyst selectivity. For the fulfillment of each one of the objectives, experiments were planned and performed as outlined in Table 1-1.

Table 1-1. Experimental schemes of this project

Objective	Experiment(s)	Expected outcome(s)
1	Thermal oxidation of FeCrAl alloy (A) strips and (B) fibers (SMF) at (a) isothermal and (b) multiple stage temperatures.	Thin layer of alumina to be grown over base metal alloy.
2	Characterization tests (a) DSA, (b) XRD, (c) XPS, (d) SEM on the developed thin layer of alumina.	Identification of the optimum support geometry and the oxidation condition (Time, Temperature) to achieve that.
3	(a) Ultrasonic adherence test, and (b) Acid immersion test.	Mechanical and chemical stability of the developed support.
4	Incipient wetness impregnation.	Desired loading of active component (Pd) on support.
5	Reaction run at different operating conditions.	Identification of the reaction operating condition regime within which mass transfer limitation is negligible and construction of reaction profiles.

The main contributions of this research were:

- 1) Fabrication of a new arranged catalyst support exhibiting no mass transfer limitation.
- 2) Drastic change in wettability of *metal oxide ceramics* with morphology.
 - Provisional US Patent (Title : *Wettability of Thermally Grown Aluminum Oxide : Mimicking the Lotus Leaf*”, S/N : 61/304,137, Inventor : John A. Nychka and Jadid E. Samad, Feb 12,2010 [94]).

Chapter 2

Important features of three phase hydrogenations

2.1 Three phase hydrogenation

Hydrogenation, as the name suggests, is the type of chemical reaction that constitutes the addition of hydrogen to another substance. Ever since people realized that with rare exception, no reaction below 480°C occurs between H₂ and organic compounds unless a metal catalyst is being used, the idea of employing catalysts in the Hydrogenation process gained much popularity. Inclusion of solid catalysts into a hydrogenation reaction system means all three phases are present in the reaction medium e.g., hydrogen (gas), hydrocarbon (liquid) and catalyst (solid), hence the name ‘three phase hydrogenation’.

2.2 Heterogeneous catalysts

Platinum group metals (Pt-group), particularly platinum, palladium, rhodium and ruthenium, form highly active hydrogenation catalysts [1]. Other metal catalysts (e.g., Ni, Mo, Co) though developed as economical alternatives, often require higher temperatures and exhibit lower selectivities than Pt-group metals. This problem is addressed by using bimetallic rather than monometallic catalysts as the former offer better stability, activity and selectivity [2]. As such, combination of two metals e.g., Ni-Mo, Co-Mo have gained wide acceptance particularly in refinery applications in the presence of sulfur. However, selection of catalyst for a particular treatment is made based on what is most important to achieve for that particular treatment. For example, catalytic cracking catalysts are chosen so that they enable major consumption of hydrogen, while also removing sulfur whereas for normal hydrotreating reactions it is beneficial to reduce the consumption of hydrogen per mole of sulfur removed [3].

2.2.1 Catalyst support

Catalytically active materials contribute to the reaction through their surfaces, which is why they are manufactured as small particles to achieve high surface area. Smaller particles, particularly those of metals, are often prone to sintering at relatively lower temperatures [4]. One widely applied method to address this is to disperse and then stabilize the active component particles on the surface of a preexisting support material. Some of the major advantages of having a catalyst support are:

- 1) Improvement of mechanical properties of the catalyst (e.g., hardness, resistance to crushing and erosion).
- 2) Higher dispersion of the active component.
- 3) Enhanced stability against sintering.
- 4) Maximum use of active phase.
- 5) Cost reduction even when active metals are expensive.
- 6) More thermal control in case of exothermic reactions.

In mostly any catalytic system support materials are used to serve as a vehicle to hold and keep the active metal particles separated in the reaction environment. Despite that support materials often go as far as interacting with the active phase to some extent. Carbon and single or mixed metal oxides such as alumina, silica, magnesia, titania, zirconia and aluminosilicates are some of the most commonly used supports in hydrogenation reactions. They are also best suited to perform all or most of the functions stated above. Al_2O_3 is used for hydrotreating catalyst supports and hence was chosen for this project (to be discussed in further detail in Chapter 4).

2.2.2 Integrating active components with support

Incorporation of active component(s) is generally achieved by bringing an appropriate precursor solution containing the active component(s) into contact with a pre-existing support. A sufficiently high interaction, which is generally of an electrostatic nature,

between them will ensure proper distribution and dispersion of the active phase on the support surface. Otherwise, poor interactions may result in unwanted distribution of active component in the form of the broad particle size distribution [4].

2.2.2.1 Chemistry of precursor solution

In a precursor solution metal cations are dissolved in water and form partially covalent bonds. This transfer of charge enhances the positive charge on the hydrogen atoms of the coordinated water molecules, thereby increasing their acidic character, which facilitates hydrolysis.

2.2.2.2 Surface charge of supports in solution

Most oxide supports are hydroxylated or hydroxylate upon immersion in water [4,5]. Under normal conditions dissociative adsorption of water molecule creates an adsorbed layer of surface hydroxyls. Such surfaces can become charged if surface hydroxyl groups dissociate or surface dissolution and readsorption of metal hydroxycomplexes take place [5]. Since both the processes involve H^+ and OH^- it is evident that pH of the solution would play a major role deciding the net surface charge. For example, in an acid solution it is most likely that the surface would be positively charged due the excess of bound protons (Eq 2-1), whereas for an alkaline solution the surface would most evidently assume negative charge (Eq 2-2). This indicates that at an intermediate pH value there will be no net charge on the surface, which is called zero point of charge (p^{Zc}) or (often loosely) iso-electric point (IEP).



Of the common support oxides alumina, titania, silica and chromia are amphoteric i.e., they adsorb cations in alkaline and anions in acid solution. So when $pH < p^{Zc}$ such oxide particles would tend to adsorb anions like $PdCl_4^{2-}$ to compensate positive charges on their surfaces, whereas at $pH > p^{Zc}$, the same surface would be more drawn towards cations like $Pd(NH_3)_4^{2+}$. Nevertheless there are other oxides for which IEP is so low that they adsorb cations (e.g., zeolites) only or so high that they adsorb anions (e.g., magnesia) only.

2.2.2.3 Different impregnation techniques

a) Co-precipitation

A solution mixture of catalytically active component and support material is dried, calcined and finally reduced to coprecipitate a porous material that will have a very high surface area. Precursor solution often suffers from reduced reducibility when co-precipitation is used to prepare metal-based catalysts. This can ultimately reduce the availability of active components [6]. Moreover, support materials e.g., alumina prepared via this method may be dissolved under strong acidic or basic conditions. Nevertheless, this method is generally applied for inexpensive materials where optimum catalytic activity is a priority. Ni/Al₂O₃ for steam reforming and Cu-ZnO/Al₂O₃ in the synthesis of methanol are few examples of coprecipitated catalysts [7].

b) Precipitation and Impregnation

Both methods comprise of filling up the pores of preexisting support materials with precursor solution containing the catalytically active element. Consequently the solvent is removed by drying. These are preferred methods when catalyst precursor is expensive and deposition in the form of nanometer sized particles is an objective. These methods are simple and high loadings of active phase can be achieved. However, a homogenous distribution of active components is often difficult to achieve because of the difficulty in the drying stage [8]. Moreover, for salts having low melting points, such as, deposition of Ni using acetate or nitrate, poor distribution of active sites results upon heat treatment [9,10]. For such cases deposition-precipitation technique is preferred. Nevertheless, oxide-supported catalysts are generally prepared via impregnation [9,11].

c) Deposition-precipitation

In this method, support material in the form of powder is suspended in the precursor solution. At their interface crystallites of metal hydroxide or carbonate precipitate via heterogeneous nucleation. After that, the solid is filtered off, dried, and shaped in subsequent stages. For low melting point salts e.g., nitrate or acetate this method is

preferable as it yields more homogeneous dispersion of the active sites than impregnation [8].

2.2.3 Effects of particle size and support texture

As discussed in the previous section, surface area is one of the most critical parameters of catalyst supports and hence should be given due consideration during support selection. Some processes require high surface area supports (e.g., hydrogenation, hydrodesulphurization) whereas other processes may work well with low surface area (e.g., olefin epoxidation). For systems where the active phase is too active and may run the risk of unwanted secondary reactions, nonporous low surface area supports are used. These supports ensure high selectivity via short contact times. Otherwise, porous and high surface area supports are desirable. In porous supports, pore characteristics (size, shape, tortuosity, connectivity) can significantly affect catalytic performance and hence should be given careful consideration. In practice, support materials, in the form of micro and millimeter sized powders are not used. For a fixed bed reactor where materials undergo tremendous pressure or for a fluidized bed reactor where materials, if small, run the risk of being blown out of the reactor, it is imperative that catalysts be shaped into larger bodies. Some common shapes are spheres, granules, pellets or large aggregates like ceramic rings and honeycomb monoliths. Oxide materials commonly used as supports generally have surface areas of 50 m²/g or higher [5].

Many catalytic hydrogenation reactions show sensitivity to the size of nanoparticles as both selectivity and turn over frequency (TOF) tend to change for these reactions. This occurs probably due to electronic and/or geometric effects [2,12]. For gas phase hydrogenation of vinylacetylene catalytic activity has been shown to reduce with decreasing the size of Pd particles. Also, for hydrogenation of acetylene TOF increased with increasing particle size of deposited Pd from 8-13 nm [13].

From the discussion above it is evident that a catalyst development encompasses many length scale.

2.3 Action sequence in three phase hydrogenation reaction

Any solid catalyzed reaction commonly consists of the following steps (Figure 2.1):

- 1) Diffusion of reactants from bulk to the external surface of the catalyst (external diffusion).
- 2) Diffusion of reactants through the pores to the active sites (internal diffusion).
- 3) Adsorption of one or both reactants on active sites.
- 4) Reaction on support surface between adsorbed species or between surface species and a reactant in the fluid phase.
- 5) Desorption of product from support surface.
- 6) Diffusion of products out of the pore and into the external fluid.
- 7) Diffusion of products away from the catalyst to the bulk.

For such reactions, it is likely that any one or several of these steps will become the rate limiting step(s).

Rate of a catalyzed reaction depends on the concentrations of the reactant at the catalyst surface. As can be seen in Figure 2.1 concentration value at the catalyst surface does not remain same as bulk ($C_{H_2,liq}$ compared to $C_{H_2,s}$). The effective rate of such reaction depends on many underlying parameters, such as, temperature, characteristics of phase boundary, structure of pores, size and bulk density of catalyst and the transport rate in the diffusion boundary layer. In order to fully exploit the capacity of a catalyst and to describe the reaction mechanism of a catalyzed reaction in the terms of rate equations it is imperative to ensure that mass transfer (steps 1,2,5,6) is not the rate limiting step. In the subsequent chapters ways to eliminate external (steps 1 and 7) and internal (steps 2,6) mass transfer limitation will be discussed.

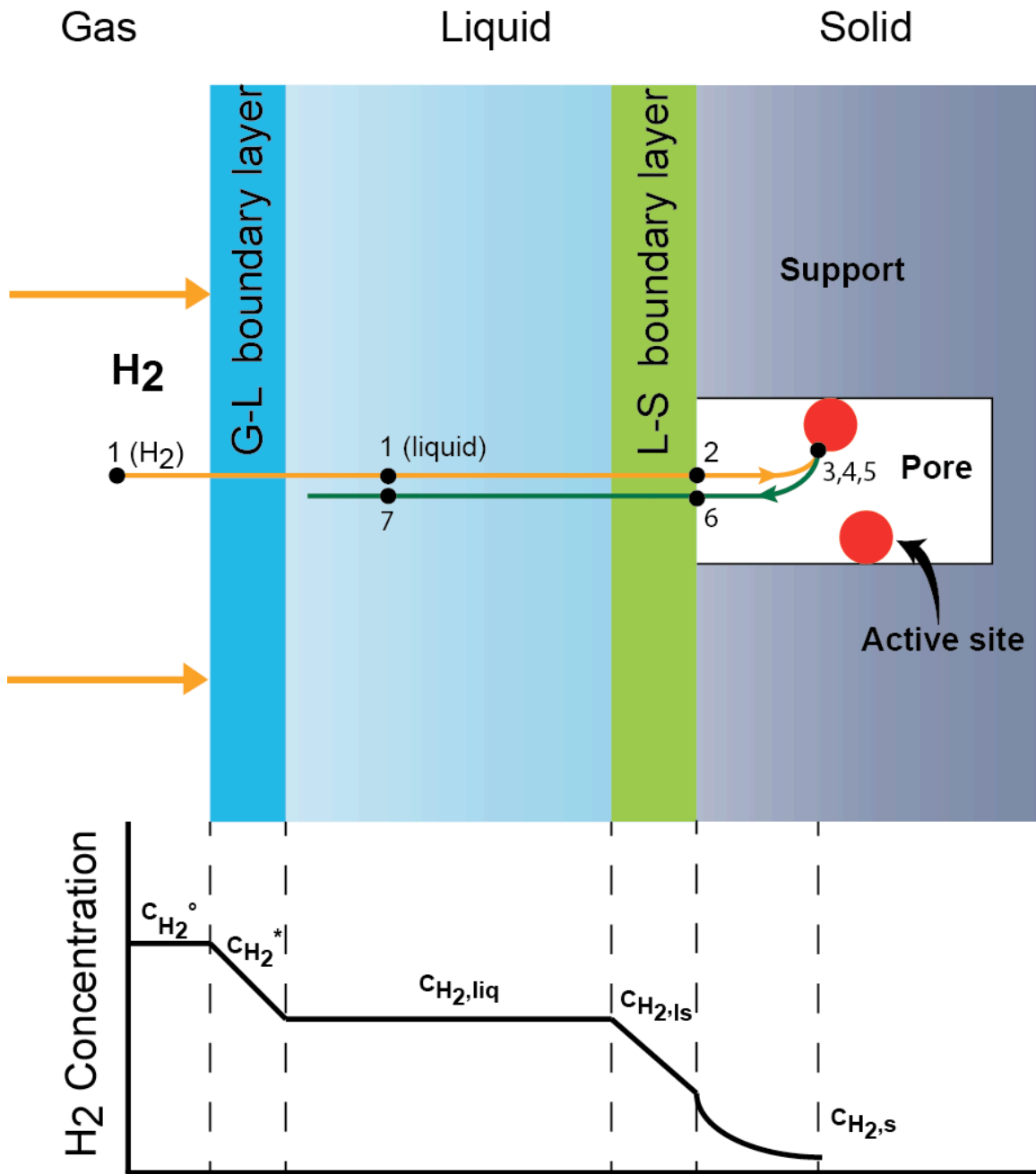


Figure 2.1. Steps of three phase hydrogenation reaction.

2.3.1 External mass transfer (film diffusion)

Mass transfer of reactants from bulk to the external surface of catalyst falls into this category. Hence in a three phase reaction it will include (a) gas-liquid mass transfer and (b) liquid-solid mass transfer.

a) Gas-Liquid mass transfer

For a typical hydrogenation reaction, H₂, as a gas, must overcome the dissolution barrier to dissolve in the liquid phase. Applying Henry's law for dilute solutions, the saturation concentration of hydrogen in the liquid phase can be correlated with partial pressure of Hydrogen according to the following formula:

$$C_{H_2}^* = \frac{P_{H_2}}{H_{H_2}} \quad (2-3)$$

Where H_{H_2} [Pa.m³.mol⁻¹] is the Henry's coefficient for hydrogen in a dilute solvent at fixed temperature.

Consequently, concentration of hydrogen will further go down according to the following formula as hydrogen diffuses through the bulk liquid (Figure 2.1).

$$m_{gl,H_2} = k_l a_l (C_{H_2}^* - C_{H_2,liq}) \quad (2-4)$$

Here, m_{gl,H_2} [mol.m⁻³.s⁻¹] is the gas-liquid mass transfer rate and k_l [m.s⁻¹] is the mass transfer coefficient of hydrogen. a_l [m⁻¹] is the gas-liquid volumetric surface area. k_l depends on the turbulence of the system as well as diffusivity of hydrogen.

b) Liquid-solid mass transfer

In the subsequent step, both the reactants have to travel from bulk liquid through the solid boundary layer to the external surface of the catalyst. This will take place according to the following equation:

$$m_{ls} = k_s a_s (C_l - C_s) \quad (2-5)$$

Here, m_{ls} [mol.m⁻³.s⁻¹] is the liquid-solid mass transfer rate and k_s [m.s⁻¹] is the liquid-solid mass transfer coefficient of the reactant. a_s is the volumetric external catalytic

surface area. C_l and C_s are reactant concentration in the liquid and at the catalyst surface respectively.

External liquid-solid mass transfer limitations exist when [14]:

- 1) Activation energy is too low (5-15 kJ/mol).
- 2) Rate and selectivity change with turbulence of the system.
- 3) Carberry number (Ca), which is the ration of observed reaction rate to maximum mass transfer rate, is higher than 0.05 [15].

$$Ca = \frac{R_{obs}}{R_{max}} = \frac{R}{k_s a_s C_{H_2,liq}} \quad (2-6)$$

2.3.2 Internal Mass Transfer

Internal mass transfer regime starts once the reactants enter the pores. To study this regime it is important to know the nature of pores. In a straight capillary pore, transport occurs in various modes. Bulk and Knudsen diffusion are two important modes that are often used in the interpretation study of internal diffusion. Bulk diffusion applies for wider pores (pore radius > 200 Å) where diffusion is independent of pore structure. In case of bulk diffusion Fick's law can be used just as in the study of external mass transfer. However, if pores are too narrow (pore radius < 50 Å) then Knudsen diffusion applies [16], where pore walls affect the diffusion process significantly as molecules would then collide more with pore walls than with one another.

Internal mass transfer can influence mass transfer when [14]

- 1) Reaction rate and selectivity change with particle size.
- 2) When reaction rate (R) changes with loading (L) as $R \propto L^{1/2}$.
- 3) A Wheeler-Weisz group is smaller than 0.1 [17]. A Wheeler-Weisz group is the ratio between observed reaction rate and maximum effective rate of internal (pore) diffusion, which can be expressed in the form of following formula:

$$WW = L_p^2 \times \frac{R \times \rho_s}{D_{eff} \times C_l} \quad (2-7)$$

where L_p is pore length, D_{eff} [$m^2 \cdot s^{-1}$] is the effective diffusion coefficient inside the pores of the catalysts ($D_{eff} = D\varepsilon/\tau$, D is the diffusion coefficient in the liquid, ε is the porosity and τ is the tortuosity factor). Industrial catalysts often show internal mass transfer limitation which makes it difficult to mimic the performance of industrial reactor for scale up purposes [18].

2.4 Catalyst deactivation

A deactivated catalyst exhibits significant change in the activity and/or selectivity of the process. It is imperative to understand the causes of deactivation in order to achieve control. Some of the most common deactivation modes are discussed briefly below:

2.4.1 Poisoning

Poisoning of catalysts occurs when specific components in the reactant feed strongly adsorb via chemisorption onto the active sites and block reactant access. Some elements of group VA, VIA and VIIA (e.g., N,P, As, Sb, S, F, Cl, Br) and some heavy metals and their ions (e.g., As, Pb, Hg, Cu, Fe) are notable catalyst poisons [12]. Moreover, adsorbed poison may bring about considerable changes in electronic or geometric structure of the surface [12]. Nevertheless poisoning can also have beneficial effects. Sometimes catalysts are deliberately poisoned in order to reduce the activity towards an undesired reaction. As for example, during hydrodesulfurization of petroleum feedstock the catalysts often are presulfided so that the activity is reduced, which will minimize the production of some unwanted gases [13].

2.4.2 Deposition of coke and/or inactive metals

Coke and/or some inactive metal may physically deposit onto catalyst surface, significantly at the pore entry and reactor voids, which may lead to the loss of activity via

complete blockage of pores and sites. Coke containing precursors, e.g., olefins or aromatics, if used in cracking reaction form coke on oxide or sulfide catalysts [12].

2.4.3 Sintering and leaching of active components

In order to maximize the number of active sites, smaller particle size is necessary as this will render high surface to volume ratio. However, surface molecules belong to higher energy states and hence are thermodynamically unstable. As a result, smaller crystallites having a considerably higher surface to volume ratio are most likely to aggregate to reduce the ratio and thereby reach a favorable low free energy state [13]. This phenomenon most frequently takes place at elevated temperatures which results in reducing the active surface area and thereby activity too. Although sintering at low temperatures is mostly restricted to unsupported catalysts some documented reports on sintering at room temperature are also available [19]. On the other hand, leaching can significantly cause deactivation of catalysts in liquid media. For metal catalysts, leaching depends on the properties of reaction medium, bulk and surface metal. Leaching of the support can also be a primary cause of metal loss. Some widely used catalyst supports, when used in organic reactions, tend to dissolve in acidic and chelating medium [15].

2.4.4 Mechanical failure

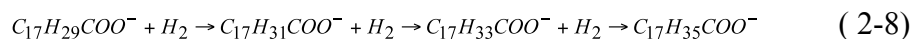
Mechanical failure, in the forms of, crushing, attrition and erosion, may induce catalyst loss and thereby the activity. These failures take place, mainly due to high fluid velocity and/or heavy load in the reactor. Formation strategies of some commercial catalysts often make them susceptible to mechanical failure. Catalyst granules, sphere, extrudates are generally prepared by agglomeration of much smaller primary particles (10-100 nm) into larger aggregates. These aggregates tend to have lower strength than the primary particles [20]. Unlike some other deactivation modes, mechanical failure may lead to drastic catastrophic consequences.

2.5 Applications of Hydrogenation reaction

Hydrogenation is said to be the most widely used reaction in organic chemistry and its related industry [1]. Some common, yet immensely significant applications of hydrogenation systems are briefly discussed in the following paragraphs.

2.5.1 Food industry

Vegetable oil is the major source of edible oil in the world. For bakery needs this type of oil often has to be ‘hardened’ via hydrogenation reaction in presence of catalyst (Eq 2-8) [21].



Linolenate Linoleate Oleate Stearate

Number of double bonds: 3 → 2 → 1 → 0

Catalysts used for these type of reactions are mostly Ni, Pd or Pt based [21].

Due to health benefits of unsaturated oils/fats over saturated ones and some health hazards of trans fatty acid (TFA) [22], research interests have grown considerably towards optimizing the level of hydrogenation (partial hydrogenation) in order to have the desired texture (hardness) without causing health concern [23,24].

2.5.2 Petroleum industry

Most often the hydrocarbon feedstock in petroleum refineries contains a considerable amount of heteroatoms and metals, specifically sulfur, nitrogen, vanadium, which may cause concern for the environment as well as the catalyst itself [1,25,26]. The removal of heteroatoms can be achieved by hydrotreating, i.e., hydrodesulfurization (Eq 2-9). Due to more stringent emission standards research on deep desulfurization techniques is also given more emphasis nowadays [26,27].

Besides, there exists heavy demand of fuel which evoked a growing dependence on heavy oils and residua. These heavy fractions can be cracked using hydrogen at elevated pressure in presence of a catalyst to transform them into low boiling point compounds.



Combination of active metals and support is often used as catalysts. Some widely used hydrotreating catalysts are CoS-MoS₂, NiS-MoS₂, NiS-WS₂, PdS on Al₂O₃ or zeolite supports [3].

Chapter 3

Structured Reactors

Conventional fixed bed catalytic reactors have long been the obvious choice for different catalytic industries. However, these traditional reactors have some obvious shortcomings, some of which are:

- 1) Large pressure drop.
- 2) Maldistribution of reactants with catalyst.
- 3) Easily fouled by dust.
- 4) Randomness of the bed which complicates scale up, modeling and design.
- 5) Less number of degrees of freedom i.e., less control during design to find the most optimized conditions.

Structured reactors were introduced with the promise to address these drawbacks. As the name suggests, these types of reactors contain regular structure of catalysts free of the randomness unlike the more conventional fixed bed. Three basic types of structured reactors are usually discussed in literature: Monolithic, Membrane and Arranged reactors [6].

3.1 Monolithic Catalysts

Monolithic structures are comprised of parallel passages made out of unit blocks of small metal or ceramic (0.5-4.0 mm). Active compounds are either uniformly spread over the entirety of the porous monolithic structure (incorporated type) or are placed upon a layer of porous materials deposited on channel walls (washcoated type). Shapes of the channels or passages may be square, sinusoidal, circular, hexagonal or triangular.

3.1.1 Main features

1. Due to its open structure it can allow high flow rate with less pressure drop (one order of magnitude less than trickle bed).
2. Absence of mass transfer (internal and external) limitation due to:
 - very high gas-liquid contact area.
 - short gas-liquid diffusion lengths (Figure 3.1).
3. Higher activity, stability and selectivity are attributed to excellent mass transfer characteristics.
4. In the preferred flow pattern (discussed in detail in 3.1.2) in monolithic reactors liquid slugs are kept separated by the introduction of gas slugs (Figure 3.1). In between these gas slugs and the channel wall there exist a thin liquid layer. This ensures proper radial mixing within the slugs of liquid. Besides, a very thin liquid film provides monolithic catalysts some advantageous by ensuring that:
 - a high contact area is available between phases for improved mass transfer characteristics.
 - the axial dispersion remains low (no bypassing).
5. Scale-up of reactor is easier as only numbering up of the unit blocks is enough [28].

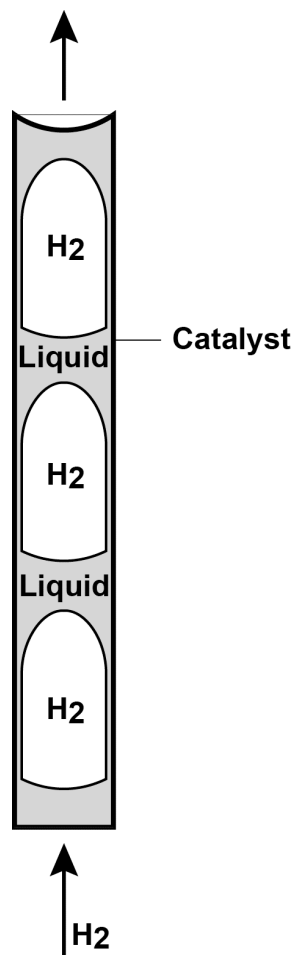


Figure 3.1. Schematic of Taylor flow in Monolithic reactor for three phase hydrogenation system.

3.1.2 Monoliths in multiphase reactions

Even though monolithic reactors hold clear advantage over conventional catalysts especially in multiphase reactions, application of monoliths in this particular sector still remains limited [31]. Only large scale application of monolithic catalysts in multiphase reactions could be found in the production of hydrogen peroxide using anthraquinone process [30]. However, a good number of research efforts are already in place to change this trend [29]. Monolithic catalysts used in hydrotreating reactions have been studied [32-35] and also their use in other hydrogenation reaction systems has also been addressed in literature [36-39]. Theoretical and experimental comparisons between conventional and monolithic reactors in three phase application have already been

conducted in terms of their typical parameters [32,40,41]. These studies reveal superior behavior of the monolithic reactor [29,40,41]. However, proper distribution of reactants including redistribution inside the reactor is something that is still under development for monolithic reactors [40]. Improvement of reactant distribution in monolith reactors has been discussed extensively in literature [36,40,42]. Monolithic reactors preferentially require high surface area materials and higher cell density. Some other problems are high manufacturing cost, poor heat transfer for ceramics, short residence time and detachment of active layer by thermal stresses [6].

3.1.3 Two phase flow patterns in capillary monoliths

As has been already discussed in the previous sections, the structure of monolithic reactors comprises of channels. Two phase flow through these channels will be largely influenced by their size [6,31]. Whereas for considerably wider pores liquid will trickle downward along channel walls and gas bubbles will move through the core of the channel. From uniform distribution standpoint this may not be ideal. Hence often it is preferred to maintain capillary channels in monolithic reactors for which elongated gas bubbles cover almost the entire channel except for the channel walls. Thus liquid slugs remain separated by gas bubbles that facilitate mixing (Figure 3.1). On top of that presence of a thin liquid layer in between gas bubbles and the channel wall ensures high contact area for multiphase mixing, keeps diffusion length short and minimizes axial dispersions. Length of bubble and slug can be changed by varying inlet condition [31]. This flow pattern, known to be as Taylor, segmented, plug or slug flow, is found to be the most ideal for multiphase distribution [6,36,42]. Studies have also been performed to understand the threshold size for capillary channels [31].

3.2 Membrane Catalysts

Membrane catalysts are one type of monolithic catalyst, additionally having permeable channel walls for improved radial mixing. The catalysts of this kind are mainly deposited on or inside of the channel walls allowing diffusion to occur through the pores of these permeable walls. Membrane can either be made of metals or inorganic compounds. Most

of the metallic membranes used in chemical reactions involving hydrogen as reactants are either Pd based or made by coating different support with thin layer of Pd or other metals. On the other hand inorganic membranes are either supported (asymmetric) or unsupported (symmetric).

Main Features

1. Improved radial mixing of reactants as well as energy which can enhance:
 - Reaction rate.
 - Selectivity.
2. Competing adsorption of reactants is common for conventional reactors, resulting in decreased reaction rates. A membrane having selective permeability for one of the reactants provides the opportunity to independently control surface concentration of the reactants, thus competing adsorption of reactants can be suppressed.
3. By facilitating differential addition of oxygen membrane reactors can nullify the risks of hot spots and explosions [43].
4. In cases where the liquid phase reactant is viscous and/or has a low solubility for the gas phase (e.g., saturation of vegetable oil), one or more reactants could become scarce at the catalyst surface leading to slowing down of the reaction rate and/or inflicting detrimental effects on the products (e.g., formation trans fatty acid in heavy oil saturation). This can be addressed by using a membrane reactor system that would facilitate supply of reactant at the catalytic sites [44].

3.2.1 Membrane reactors in multiphase systems

In hydrogenation systems, preferentially those that use low hydrogen pressures, membrane reactors have been shown to perform better than conventional catalysts. Some monolithic palladium based membrane catalysts have been shown to exhibit high selectivity and reaction rate in some hydrogenation reactions [6,45]. In the production of

some various products of high purity, e.g., vitamin, drugs, hard fats and fragrances via partial hydrogenation composite membranes (a very thin palladium alloy layer on a refractory porous support surface) have also been showed to be more selective than the conventional ones.

3.3 Arranged Catalysts

Particulate catalysts that may be arranged in arrays or nonparticulate catalysts that consist of packings covered with catalytically active materials all belong to the group of Arranged Catalysts.

Main Features

1. Structural packing is one attribute of nonparticulate arranged catalysts. They often come with high voidage which guarantees low pressure drop. Intensive heat and mass transfer over the entire reaction zone is achievable. Three dimensional matrix formation of fibers can also act as static mixers and prevent channeling. Sintered metal fiber (SMF) used in this project is an example of arranged catalyst [46].
2. Particulate catalysts formed in arrays often come with three level of porosity: pore space within each particle, intraparticle space and space in between the arrays. Two examples of reactors having this three level of porosity are: (i) parallel flow reactor and (ii) lateral flow reactor [47].
3. In parallel passage reactors (PPR) gas flows through straight channels along the catalyst bed, unlike fixed bed where gas flows through the bed. Straight gas passages prevent the impingement and accumulation of particulates present in the gas. Hence PPR is advantageous in the treatment of dust containing gases. Shell flue gas desulfurization process removes oxides of sulfur from flue gas in a parallel passage reactor system [48].

4. Lateral flow reactors (LFR) are constructed similarly to PPR with the exception of the latter having gas passages closed off at one end with alternating passages open and closed at different ends. This setup forces gas to flow through catalyst layers as well. For the same reason the LFR is more prone to fouling than PPR and suffers from low mass transfer rates. However, bead string reactor is an update of LFR where mass transfer rates can be higher [47]. Shell low temperature NO_x removal process is one example of industrial application of LFR [49].

3.4 Microstructured Reactors

These reactors, containing open paths for fluids in the dimension of sub millimeter range, are relatively new addition to structured reactor system [50,51]. Main features of this type of reactor are very high surface to volume ratio (approximately 10000-5000 m²/m³) and high heat transfer coefficient [51]. As a result these microstructures are capable of maintaining faster cooling and heating, avoiding formation of hot spots and making full utilization of catalysts in case of highly exothermic or endothermic reactions. Narrow reactor channels ensure short radial diffusion time for which a narrow residence time distribution can be achieved. Scaling up is easier and necessitates only multiplication of units. Smaller set up improves inherent safety of the system. In short, microstructured reactors have the potential to be used for fast and highly exo or endothermic reactions. Some examples of the application of microstructured reactors can be found in literature, although most of which only concern laboratory scale [19,51,52]. Microchannels discussed above have several drawbacks. Randomly packed microchannels cause high pressure drop; besides identical packing of each channel is imperative to avoid maldistribution. Hence the concept of structured catalytic bed, arranged with catalyst-coated filaments or wires and placed along a tubular reactor (“string” reactor) has been proposed (Figure 3.2) [53,54,55]. For exothermic hydrogenation reactions where efficient heat transfer is a *priori*, introduction of microstructured reactors can be beneficial. Laminar flow through micro channels between the filaments renders the same advantages as monolithic reactors. Taylor flow can be attained under certain conditions for such novel reactors as well [56].

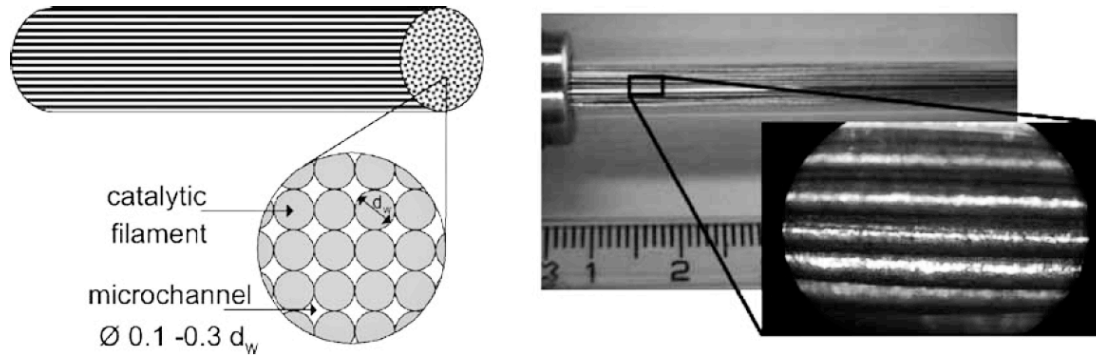


Figure 3.2. Schematic illustration and photograph of string reactor [55] [reused with permission from *Chemical Engineering Journal*]

Structured reactors can improve mass transfer in three phase hydrogenations leading to processing intensification. However, they still require development of novel structured catalyst in order to fully exploit its advantages.

Chapter 4

Alumina catalyst supports:Nature and Fabrication

4.1 Different polytypes of Alumina

As discussed in the earlier part of Chapter 2 alumina is one of the preferred choices of catalyst supports for its multifarious advantages. Different polytypes of alumina have been reported in literature e.g., $\alpha, \delta, \theta, \kappa, \eta$ [57-62]. Among them α -alumina is the most stable polytype over other polytypes which are mostly metastable. The transformation of metastable to α -alumina is irreversible. Hence, most alumina deposited as ores in nature are in the form of α -alumina (corundum).

4.2 Use of alumina as a support

$\alpha, \gamma, \theta, \eta$ -aluminas are generally used for various catalytic applications [5,62-64]. In catalytic applications where high surface area is required metastable alumina, especially γ -alumina is used, whereas for low surface area requirements α -alumina might be used for its higher mechanical and thermal stability [57-61,64]. As discussed in Chapter 2, alumina, like many other oxides, is amphoteric in nature. Hence it can exhibit Bronsted acidity, Lewis acidity and Lewis basicity and can act as cation or anion depending on the pH. γ -alumina can create mesoporosity with specific surface areas between 50 to 300 $\text{m}^2 \cdot \text{g}^{-1}$ whereas α -alumina (corundum) is nonporous with specific surface area $\sim 3\text{-}5 \text{ m}^2 \cdot \text{g}^{-1}$ [64] Although γ -alumina renders a high surface area it often suffers from dissolution during supported catalyst preparations, rehydration during catalyst implementation because of H_2O production and thermal degradation upon catalyst regeneration [65].

On the other hand, α -alumina, in addition to having lower surface area (than γ), is more stable against hydroxide ions and less acidic [62]. However, it can provide less active sites for undesirable product formation [62].

4.3 Preparation of Alumina support

Porous alumina can be manufactured by controlled dehydration of aluminum hydroxide ($\text{Al}(\text{OH})_3 = \text{Al}_2\text{O}_3 \cdot 3\text{H}_2\text{O}$) or aluminum oxide hydrates ($\text{AlOOH} = \text{Al}_2\text{O}_3 \cdot \text{H}_2\text{O}$). Non porous aluminum oxide exists in various crystalline forms as gibbsite, bayerite and nordstrandite. Thermal treatment of Gibbsite yields bohemite with high surface area. Further treatment between 400°C and 1000°C yields a series of porous crystalline transition alumina e.g., $\kappa, \delta, \theta, \gamma, \eta$ -alumina. However, calcination above 1000°C yields crystalline non porous α -alumina [64].

4.3.1 Alumina formed via thermal oxidation

Some Al-containing alloys form alumina upon thermal oxidation [57-61,66,67]. During this process, which is also known as selective oxidation, Al readily diffuses to the surface and reacts with oxygen in the air to form alumina [59,66,67]. The nature of the polytype of alumina thus formed would depend on several conditions e.g., oxidation time, temperature, presence of reactive elements and type of alloy used. Temperature ranges within which metastable alumina is formed depend on thermal treatment and crystallinity and impurities present on base metals [68]. At temperatures greater than $\sim 1000^\circ\text{C}$ a compact, adherent and inert α -alumina forms whereas at temperatures lower than that other metastable alumina polytypes predominantly form on the surface. Although metastable aluminas are reproducible and significantly stable at room temperatures, the transformation sequence from metastable to stable α alumina is irreversible [57-61,66,67].

During initial periods of oxidation at temperatures within the metastable alumina forming zone [69], platelets and/or whiskers of metastable alumina form. The scale growth rate is considerably high during this stage as platelets rapidly cover the entire scale surface. The mechanism of their growth has been speculated to be due to enhanced diffusion along particular crystallographic directions via impurities as well as their different crystallography compared to α -alumina. As a result a quick surge of weight gain takes place during this stage [59]. After hours of oxidation, multiplication of platelets tends to

slow down and underlying stable α -alumina layer initiates. At this interim stage a mixture of stable and metastable alumina may exist. Incidentally at longer oxidation times the surface becomes fully covered with stable α -alumina.

Aspect ratio of whiskers or platelets can be regulated via changing processing conditions (time and temperature). From thermodynamics it is established that at lower temperatures there are more nucleation sites. However, at higher temperatures the growth is faster. In order to have a higher aspect ratio of whiskers or platelets staged oxidation can be used, where oxidation initiates at lower temperatures to facilitate forming nucleation sites and later after some time temperature is raised to ensure higher growth rate.

4.4 Effects of Reactive elements on the oxidation process

Different reactive elements (e.g., Zr, Y, Ti, Mo, Ce) present in the base metal alloy can markedly influence the oxide scale growth mechanism. Yttrium, hafnium and cerium improve the adhesive strength of the scale [66,70], the mechanism of which is still not completely understood [58,71]. Also numerous studies have suggested that such elements may hinder or accelerate the transformation from metastable to stable alumina [57,66,67], probably depending on which of the roles they play [66]. Elements like Y, Ce reportedly work both ways in affecting the transformation process [63,66,72-75]. Some reports proposed that the presence of larger ions would hinder the transformation whereas smaller ions would accelerate it [67]. Considerable doubts still remain regarding the mechanism that these reactive elements follow to influence the transformation process. However, their influence becomes less noticeable at higher temperatures ($\sim 1200^\circ\text{C}$) at which stable α -alumina predominantly forms regardless of their presence [66,75]. Nevertheless, the study of reactive element influence on oxidation behavior of alumina forming alloys will continue to attract interest of the researchers as for different applications ensuring the stability of either metastable [63,76,77] or α -alumina may be necessary [57,70].

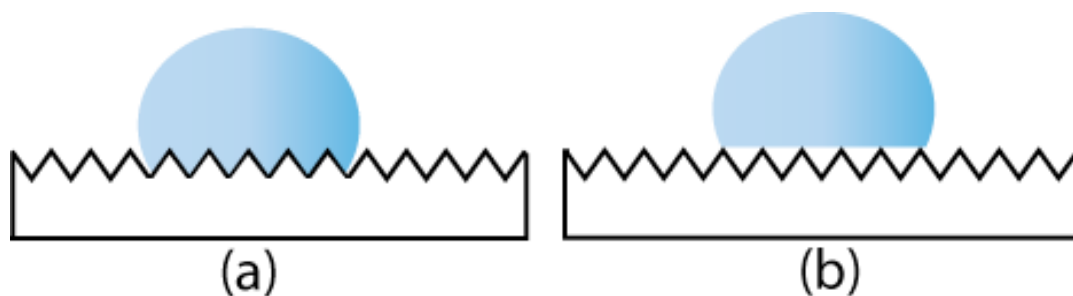


Figure 4.1. Different wettability modes: (a) Wenzel and (b) Cassie-Baxter.

4.5 Wettability of alumina

In order to ensure uniform dispersion of active sites on the support surface, it is necessary that the precursor solution completely ‘wets’ the surface. Hence knowing the wettability of the surface can be crucial information to have that may influence the selection of precursor solutions. The vast morphological changes that an alumina forming alloy undergoes upon oxidation at high temperatures can also affect the wettability trend of its surface [78-81]. Besides, considerable difference in surface energy values between different alumina polytypes reported in literature can also favor wettability change. Presence of transition alumina, many of which have morphology resembling whiskers/platelets, may trigger wettability change via Wenzel or Cassie-Baxter mode (Figure 4.1), both of which will be discussed next.

4.5.1 Influence of roughness on wettability

For the case of the Wenzel state, roughness triggers an increase in surface area. So, the contact angle (Θ) obtained from Young’s equation has to be modified for the rough surface in the following manner:

$$\cos \Theta' = r \cos \Theta \quad (4-1)$$

where, r is the ratio of actual to projected surface area ($r > 1$ for Wenzel State) and the apparent contact angle is Θ' . According to Eq 4-1, roughening can render a hydrophobic

surface more hydrophobic and a hydrophilic surface more hydrophilic. In short, roughness plays only the role of an amplifier without the ability to alter trends in intrinsic wettability (i.e., wettability based on surface free energy).

In the Cassie-Baxter state the liquid drop forms on a composite interface, comprising of liquid-air, solid-air and liquid-solid interfaces. Here the droplet does not maintain full contact with the solid, unlike in the Wenzel state. Eq 4-2 demonstrates how the apparent contact angle is affected by the Cassie-Baxter state on the composite surface:

$$\cos \Theta' = f_{sl}(1 + \cos \Theta) - 1 \quad (4-2)$$

Here f_{sl} is the fraction of the droplet surface in contact with the solid ($f_{sl} < 1$ for Cassie-Baxter state). This equation implies that in addition to acting as an amplifier, roughness can also alter the trend in wettability. As a result, according to this model, an apparent hydrophobic surface is achievable from a hydrophilic surface if the roughness of the hydrophilic material is significant and $f_{sl} \ll 1$. Such implications have given rise to many investigations in the field of textural surface modification to achieve superhydrophobicity.

Ceramics, such as, alumina are intrinsically hydrophilic nature [83]. Hence, formation of whiskers or platelets would either amplify (Wenzel State) or alter (Cassie-Baxter State) wettability trend. However a state intermediate to both Wenzel and Cassie-Baxter may also result.

Chapter 5

Experimental methods

Experimental schemes for this project have already been outlined in Table 1-1 in Chapter 1. Detail about materials, methods and underlying techniques and testing equipment will be discussed in the next few paragraphs of this Chapter.

5.1 Materials

5.1.1 FeCrAl alloy

High temperature oxidation resistant FeCrAl alloy has been used in two forms: (i) Bulk strip (Kanthal A-1, Kanthal AB, Sweden) and (ii) Sintered metal fiber, SMF (Bekipor® ST DPF 701, N.V. Bekaert S.A., Zwevegem, Belgium) throughout this project. Specifications of these two are provided in Table 5-1.

Table 5-1. Product specifications of FeCrAl strip [82] and SMF*.

Material	Metallic additions (wt%)			Other Specification	Dimensions of stock supply
	Al	Cr	Others		
Kanthal A-1 (Kanthal AB, Sweden)	5.8	22	Ti <0.3, Zr 0.1 and Balance Fe	-	30 cm x 1.5 cm x 0.3 cm
SMF (Bekipor ® ST DPF 701, N.V. Bekaert S.A., Zwevegem, Belgium)	4.2	19-22	C ≤ 0.06, Mn ≤ 0.04, Si ≤ 0.06, P ≤ 0.05, S ≤ 0.03, Cu ≤ 0.2, N ≤ 0.03 and Balance Fe	Porosity 80%, Thickness 0.3mm, weight 450 g/m ²	118cm x 154cm

*. Bekipor ® ST DTF product specification

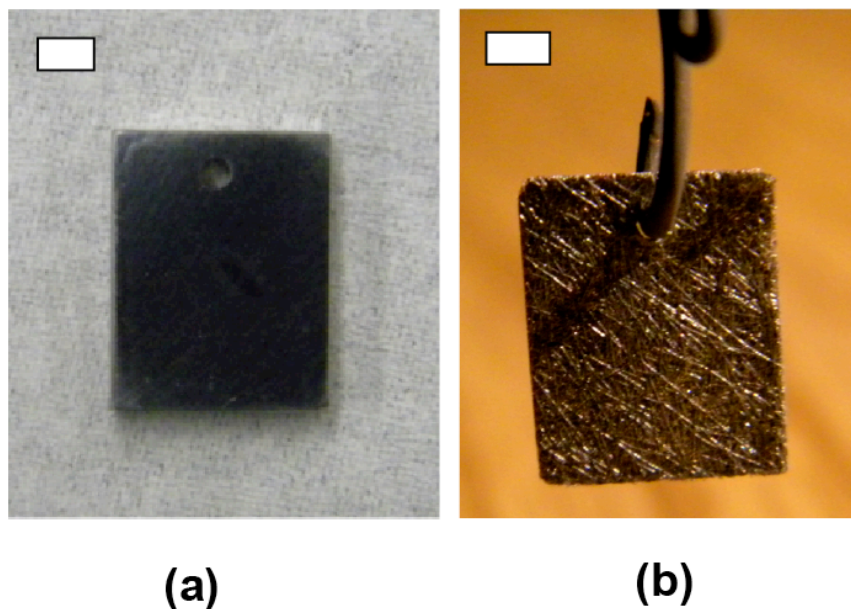
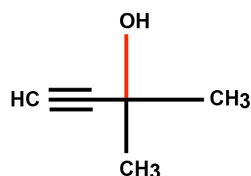


Figure 5.1. Photographic image of (a) FeCrAl strip and (b) Sintered metal fiber (SMF). Scale bar is 3 mm.

5.1.2 2-methyl-3-butyn-2-ol (MBY)

Structure:



Supplier: ALDRICH® Chemistry (Sigma-Aldrich Co., Missouri, USA)

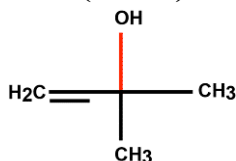
Container: 100 ml

Purity: 98%

Density, $\rho_Y = 861 \text{ kg.m}^{-3}$

5.1.3 2-methyl-3-buten-2-ol (MBE)

Structure:



Supplier: Acros Organics, New Jersey, USA

Container: 250 ml

Purity: 97%

Density, ρ_E = 820 kg.m⁻³

5.1.4 Hydrogen

Supplier: Praxair, Ontario, Canada

Purity: Ultrahigh 5.0

5.1.5 Nitrogen

Supplier: Praxair, Ontario, Canada

Purity: Zero 4.8

5.1.6 Ethanol (solvent)

Supplier: Ricca Chemical Company, Arlington, Texas, USA

Container: 4 L

Concentration: 100 parts per volume ethanol and 5 parts per volume methanol

5.1.7 Pd precursor

PdCl₂ (5%w/v)

Supplier: Acros, New Jersey, USA

5.1.8 Water

Milli-Q® water (purified and deionized water manufactured by Millipore Corporation) was used.

5.2 Oxidation

Oxidation was carried out on both FeCrAl strips (Kanthal A1) and Fibers (SMF). Due to slight differences in their processing techniques, they will be discussed separately here.

5.2.1 FeCrAl coupons (Kanthal A1)

5.2.1.1 Sample Preparation

Specimens with approximate dimensions of 1 cm x 1 cm x 0.125 cm were machined from the bulk strip using a slow speed diamond saw (Allied TechCut 4 equipped with a CBN metal bonded wafering blade). Holes (1.6 mm diameter) were drilled in the coupons so that they could be hung vertically inside the furnace. Grinding was performed using SiC grit papers (240, 320, 400, 600, 800 grit) followed by polishing through to 3 μ m polycrystalline diamond finish on an Imperial adhesive backed polishing cloth (Allied High Tech Products, Inc., Rancho Domingo, CA.). Finally the polished substrates were ultrasonically cleaned in soapy water and then acetone for 10 minutes each.

5.2.1.2 Oxidation Procedure

All substrates were oxidized in laboratory air in a high purity alumina (99.8% α -alumina) tube furnace (Barnstead International Type F21100 Tube Furnace, 1260 series). 11 specimens were oxidized at 930°C for differential length of time (15 minutes – 96 hours) and others were oxidized at two or three stage temperatures (ramp rate 40°C/min) for 4 hours in total. Various processing conditions have been chosen to analyze oxidation behavior with processing conditions as well as to find the most suitable oxide surface for support. In order to avoid contamination and to ensure that oxidation took place uniformly on all the surfaces, the substrates were hung on a polished and pre-oxidized FeCrAl wire. All specimens were inserted in and taken out from the furnace at the oxidation temperature. This was done to maximize heating and cooling rates.

5.2.1.3 Sample Preparation for scale height measurements

Oxide scales from one edge of each of the 4 oxidized specimens (t_{ox} = 15 min, 2 hrs, 24 hrs and 48 hrs) were ground off to expose the bare metal. Following grinding, the specimens were immersed in a concentrated acid mixture containing 20 ml of concentrated (36.5-38%) HCl, 20 ml of concentrated (68-70%) HNO₃ and 20 ml of H₂O (1:1:1) for 25 minutes. As a result, the edges that had bare metal exposed, corroded leaving the adjacent oxide scale intact. The specimens were then boiled in water for

another 35 minutes to dissolve any potential metal salts formed during acid immersion. Finally, the specimens were examined under SEM to characterize their fracture surfaces.

5.2.2 SMF

5.2.2.1 Sample Preparation

Due to the difficulty of grinding and polishing of mesh fibers, SMF was sectioned to size (1 cm x 1 cm). Sectioned fibers were cleaned by immersing into toluene, acetone, methanol and isopropanol subsequently. Afterwards the specimens were dried in atmosphere and weighed in a balance (Pinnacle series, Denver Instrument, Colorado, US).

5.2.2.2 Oxidation procedure

This step was same as mentioned for FeCrAl strips.

5.2.2.3 Ultrasonic adherence test

Ultrasonic treatment (Branson Ultrasonic cleaner, Model 3510, Danbury, CT) was used in order to evaluate the mechanical stability of the adhered oxide coating [46,96]. First the oxidized specimen was weighed in a balance (Denver instrument, Pinnacle series, Colorado, US), then immersed in a water container and placed inside the ultrasonic bath. Test was run for 40 minutes, after which the specimen was dried and weighed to record change in mass.

5.2.2.4 Chemical stability test

In order to check for chemical stability the oxidized SMF was immersed in a strong acid mixture consisting of 20 ml of concentrated (36.5-38%) HCl, 20 ml of concentrated (68-70%) HNO₃, 20 ml of H₂O (1:1:1). The specimen was immersed vertically using a plastic tweezer to make sure all its surface area is fully exposed to acid. The specimen was withdrawn from acid at fixed intervals and immersed into boiling water for 35 minutes to dissolve any potential metal salts formed during acid immersion. Afterwards, the

specimen was washed with ethanol and dried for another 10 minutes. Finally the dried specimen was weighed in the balance to record any change in mass and after that, immersed back into the acid mixture. The process was repeated a number of times in order to plot a mass loss profile with immersion time.

5.3 Deposition of Pd

Pd was deposited on the oxide surfaces with suitable support morphology via incipient wetness impregnation. PdCl₂ was used as the precursor solution. Bulk precursor solution (5% PdCl₂) was diluted to prepare two solutions of different Pd concentrations. These concentrations have been calculated so that the supports have the desired Pd loading after 10 immersions. In between subsequent immersions, the support surfaces were dried in oven (Fisher Scientific, Model # 3511FS, Iowa, USA) at 140°C for 20 minutes to evaporate water and some other volatile components that may be present in the precursor solution. Afterwards the deposited Pd molecules were reduced by flowing hydrogen at a flow rate of 80 ml/min (Smart-Trak2, Model 100, Sierra Instruments Inc., CA, USA) while raising the temperature to 375°C at a ramp rate 5°C/min to achieve the desired size Pd nanoparticles.

Sample Calculation (0.5wt% Pd with respect to SMF):

Average water absorption/immersion in water = 39 mg, i.e., 0.39 g \equiv 0.39 ml after 10 immersions

Average mass of SMF sample of the lot = 71.15 mg

Target loading of Pd = 0.5wt% of total SMF mass i.e., 0.36 mg

0.36 mg Pd \equiv 0.6 mg PdCl₂

0.6 mg PdCl₂/0.39 ml H₂O \equiv 0.154 g PdCl₂/100 ml H₂O

Required volume from bulk (5w/v%PdCl₂) for immersion = $\frac{100 \times 0.154}{5}$ = 3.1 ml + Add water to

make 100 ml stock solution.

5.4 Catalytic Hydrogenation

5.4.1 Experimental setup

Two three phase hydrogenation reaction schemes were studied in this project (Figure 5.2). The reactions were carried out in a heated batch stainless steel reactor (300 mL autoclave, Parr Instruments 4560 Mini Bench Top Reactor) equipped with a thermocouple, a gas burette, an internal cooling coil, one dip tube for gas admission and another for liquid sampling and a hollow gas entrainment impeller. Ethanol was used as solvent with 0.04M of MBE/MBY in a 200ml solution. The reactor was filled with the reactant mixture and support catalyst. The whole set up was then flushed with nitrogen and stirred to reach the reaction temperature. A controller (Parr 4857 process controller, PID, operating range 0-800°C, system accuracy $\pm 1^\circ\text{C}$ typical) coupled with the reactor controls the temperature via one heater. Once the desired temperature was reached the reactor was purged with hydrogen and pressurized. During the course of the reaction, the pressure in the reactor was maintained constant at 0.46 MPa absolute. The experiments were repeated two times with errors corresponding to one standard deviation. Schematic illustration of the reactor setup is shown in Figure 5.2.

5.4.2 Determination of reactants and products concentration

Hydrogen concentration in the bulk was monitored via controller pressure drop. Concentration of other reactants and products was determined from Gas chromatography (GC) analysis performed using Varian 420-GC equipped with a 30m Restek Stabilwax 0.32 mm capillary column with a 0.25 μ coating. Injector and flame ionization detector temperatures were set to be 200°C and 300°C, respectively. The oven temperature was maintained at 150°C for 4 min and then raised to 200°C at a ramp rate of 30°C/min. Mass concentrations (x_i) of different components were determined from GC Area % assuming similar GC response factors, i.e., Area % = mass%. Molar concentrations (C_i) of different components were calculated from x_i values according to Eq 5-1.

$$C_i = \frac{\frac{x_i}{M_i}}{\sum \frac{x_i}{M_i}} \quad (5-1)$$

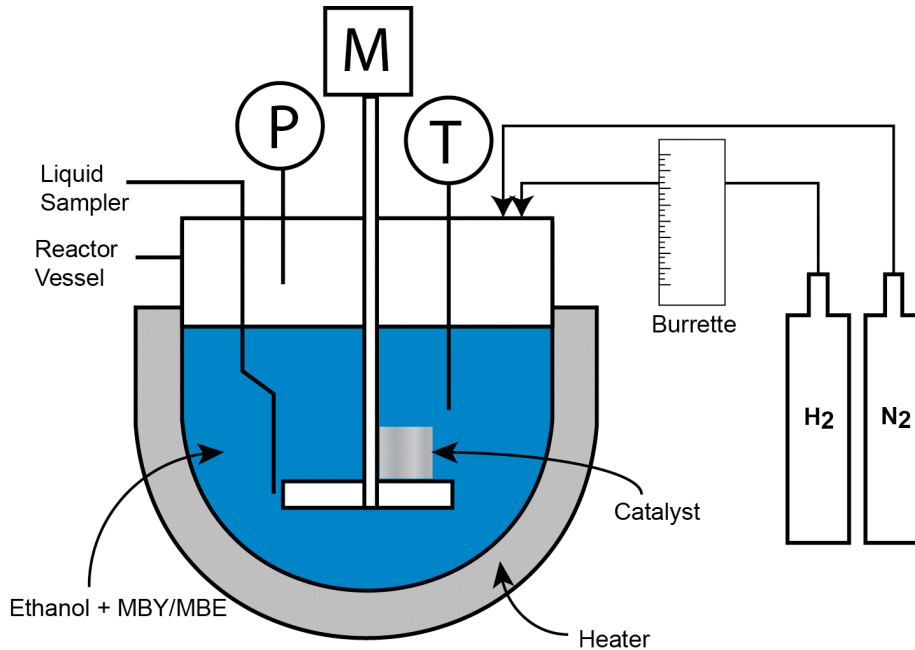


Figure 5.2. Schematic drawing of the semibatch reactor setup for three phase hydrogenation reaction using sintered metal fiber (SMF) as catalyst. This illustration is not drawn to scale.

5.5 Characterization of support catalysts

5.5.1 Drop Shape Analysis (DSA)

The sessile drop method was used for all contact angle measurements, which were taken at room temperature using a contact angle goniometer (Krüss DSA 10-Mk2, Hamburg, Germany). Image processing of the sessile water drop was done using DSA 1.90.0.14 software. At least 3 drops of 8 μL of de-ionized ultra filtered (DIUF) water were placed on 3 different locations of each sample. The water drops were allowed to settle for 5 minutes after which two contact angles were measured on each drop (the left and right hand sides of the image where the water drop contacted the substrate surface). Values thus obtained were averaged and the standard deviation was calculated.

5.5.2 X-Ray Diffraction (XRD)

XRD was carried out on a Rigaku Rotating Anode system (Thin film mode) with $\text{CuK}\alpha$ radiation ($\lambda = 1.5406\text{\AA}$) at 40 kV and 110 mA. 1° diffraction slit and 0.3° receiving slit were used. Scan speed was $3^\circ/\text{min}$. Maximum allowable sample thickness for this system is 1.5 mm. Hence, the thicker samples had to be ground off to that thickness.

5.5.3 X-Ray Photoelectron Spectroscopy (XPS)

XPS was performed on an AXIS 165 spectrometer (Kratos Analytical) at the Alberta Centre for Surface Engineering and Science (ACSES), University of Alberta. The analysis spot was $400 \times 700 \mu\text{m}^2$. Survey scans were collected for binding energy from 1100 eV to 0 with analyzer pass energy of 160 eV and a step of 0.35 eV. For the high-resolution spectra the pass-energy was 20 eV with a step of 0.1 eV. Charge neutralization was applied to compensate for sample charging.

5.5.4 Scanning Electron Microscopy (SEM)

SEM was executed on a field-emission SEM (JAMP-9500F, JEOL) at the Alberta Centre for Surface Engineering and Science (ACSES), University of Alberta. The instrument is equipped with Shottky field emitter that produces electron probe diameter of about 3 to 8 nm at the sample. The accelerating voltage for the SEM was 15 kV. The working distance was 23.8 mm.

5.5.5 Atomic Absorption Spectroscopy (AAS)

Pd loading on supported catalysts was determined using a Varian 220 FS atomic absorption spectroscopy (AAS) instrument. First a small fraction of the Pd deposited support was sectioned. The sectioned part was then immersed in a hot concentrated (60°C) nitric acid (68-70%) solution (10 ml) for 25 minutes to allow dissolution of Pd in acid. The acid solution containing Pd was diluted with water, stored inside of a 20 ml vial and sent for AAS test. Prior to AAS measurements of the actual sample a calibration curve of absorbance vs. concentration of Pd (ppm) was plotted by preparing known concentrations of Pd (0.3, 0.5, 1, 3, 5, 10, 15 ppm) from standard Pd solution (10% HCl,

1000 mg/L, 125 ml, Spex Certiprep, lot # 14-152PD, cat # PLPD3-2Y) and analyzing in AAS. Measurement of concentration of the actual solution was made based on this calibration curve.

5.5.6 Brunauer–Emmett–Teller (BET) surface area[†]

BET surface area was determined by Krypton adsorption using Quantachrome autosorb gas sorption (Quantachrome instruments, Autosorb – 1, Windows version 1.52, Florida, USA) at National Institute of Nanotechnology, University of Alberta. Prior to BET analysis the samples were degassed for 10 hours at 140°C.

[†] BET experiment was performed by Katie Krause (see Acknowledgement)

Chapter 6

Results and Discussion

6.1 Development and Characterization of new support

In order to understand the oxidation behavior, metal strips of FeCrAl alloy were first oxidized at different temperatures and time. Oxidation conditions, that were addressed, can be divided into two subcategories: (a) isothermal and (b) multiple stage (at two or more temperatures). The resultant oxide scales were characterized using various techniques explained below. Knowledge derived from the characterization tests was used to interpret the oxidation behavior of the actual Sintered metal fiber (SMF) support. These operating steps led to the identification of the most suitable support and the operating condition for the catalytic reaction addressed herein.

6.1.1 Single stage oxidation

The FeCrAl alloy strips were oxidized at $930\pm 5^\circ\text{C}$ for different lengths of time (15 minutes to 96 hours), and subsequently characterized using, in the following order (i) Drop shape analysis (DSA), (ii) X-ray diffraction (XRD), (iii) X-ray photoelectron spectroscopy (XPS), and (iv) Scanning electron microscopy (SEM). DSA was performed in order to study the influence of oxidation time (t_{ox}) on wettability at a constant temperature. Change in wettability was speculated due to the likelihood of morphological transformation of oxide scale with time. In addition to morphology the study of the wettability of the coatings will also be addressed.

6.1.1.1 Wettability of oxide scale

The water contact angle, Θ of the oxidized surfaces was measured using DSA. Average contact angle values for corresponding oxidation times had been listed in Table 6-1, along with the standard deviation. For reference, Table 6-1 lists the contact angles measured on the bare polished alloy, and an oxidized alloy surface that forms the

compact stable α -alumina. Figure 6.1 illustrates the average values plotted against corresponding oxidation times (t_{ox}); error bars are \pm one standard deviation, and shows that at the initial stages of oxidation the contact angle increased sharply until $t_{ox} = 0.5$ hr, after which contact angle did not vary much until $t_{ox} = 10$ hrs. Another drastic change (increase to 128°) in wettability was observed between $t_{ox} = 10$ hrs to $t_{ox} = 24$ hrs. The specimen oxidized for 24 hrs exhibited the maximum apparent contact angle of 128° whereas that oxidized for 0.25 hr (=15 min) showed the lowest angle of 24° . Figure 6.2 shows change in wettability behavior with formation of different alumina polytypes and change in oxidation condition.

Table 6-1. Observed contact angles for FeCrAl samples oxidized for different times.

Sample ID	Oxidation time, t_{ox} [hr]	Average static contact angle, $\Theta \pm$ standard deviation [°]
Polished FeCrAl	0	46.7 ± 2.9
Compact α -alumina*	25	38 ± 4.6
1	0.25 (=15 min)	30.4 ± 7.8
2	0.367 (=22 min)	65.8 ± 5.0
3	0.5	90.5 ± 3.3
4	1	90.6 ± 1.2
5	2	85.7 ± 6.5
6	5	72.9 ± 3.1
7	10	74.3 ± 10.6
8	17	103.3 ± 6.3
9	24	115.9 ± 9.5
10	48	113.6 ± 4.2
11	96	79.6 ± 8.7

*grown at 1200 °C

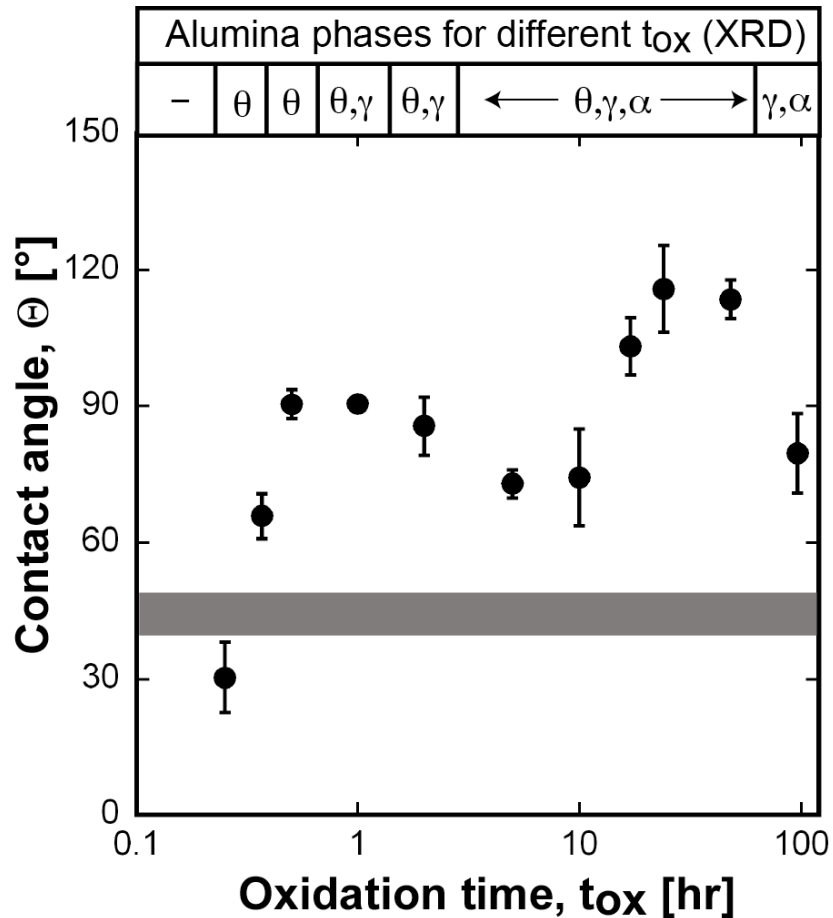


Figure 6.1. Relationship between oxidation time (t_{ox}) and contact angle (Θ) on oxidized alloy surface. XRD information on different alumina polytypes found to be present at different t_{ox} has been superimposed along the top axis. The baseline contact angle range for the unoxidized polished metal surface and compact alumina oxide scale (thermal oxidation at 1200°C for $t_{ox} = 25$ hrs) fell within the gray band around $\Theta = 50^\circ$.

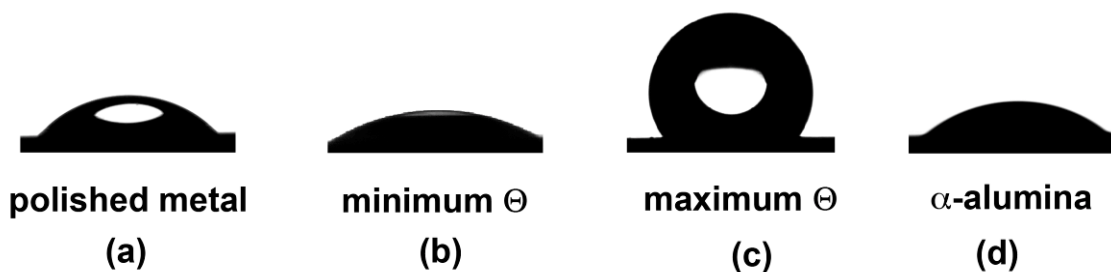


Figure 6.2. Image of ~8ml water drops on: (a) unoxidized FeCrAl alloy ($\Theta = 46.7^\circ$), (b) oxidized at 930°C for $t_{ox} = 0.25$ hr ($\Theta = 30.4^\circ$), (c) oxidized at 930°C for $t_{ox} = 24$ hrs ($\Theta = 128^\circ$), (d) oxidized at 1200°C for $t_{ox} = 25$ hrs ($\Theta = 33.4^\circ$).

(a) XRD

After observing changes in wettability, XRD analysis was performed to determine the phase(s) of alumina present on each oxidized specimen surface. From the XRD profiles, shown in Figure 6.3, it is obvious that the oxide layers consisted mainly of alpha (α), theta (θ) and gamma (γ) alumina which were found in XRD database in the form of Rhombohedral, Monoclinic and Cubic alumina respectively. Another significant observation was that whereas metastable (mainly θ and γ) alumina peaks were found predominantly at earlier stages (at $t_{ox} \leq 10$ hours) of oxidation, α -alumina was dominant at $t_{ox} > 10$ hours.

(b) XPS

XPS studies were carried out in order to check for carbon and to analyze for hydroxylation of the oxides. Carbon content was found to be similar on all 11 substrates indicating that none of the surfaces was specifically prone to carbon contamination – hence wettability trends were not due to hydrocarbon contamination of the surface. From the elemental composition obtained from XPS analysis atomic concentration ratio of O, Al and C was found to be approximately 2.5: 1.5: 1 for all the substrates. For alumina (Al_2O_3) the atomic ratio of O to Al would be 2.25: 1.5. However, the additional O found in XPS survey is due to the formation C-O and C=O bonded compounds as observed in the C1s peaks in Figure 6.4(a). After analyzing C1s peaks in Figure 6.4(a), it was found that maximum carbon was present in the form of C-C bond (~ 80%) i.e., raw carbon which may have been deposited from the atmosphere during experimentation. Also the symmetric O1s peaks (Figure 6.4b) for all 11 samples prove that no hydroxylation of the aluminum oxide ceramic coatings formed in any of the samples [83]. Presence of Hydroxyls can reduce the wettability of alumina probably by passivating the acid-base sites on the surface which eventually results in a lower overall surface free energy [83]. The XPS results excluded the possibility of such hydroxylation effect occurring in this case.

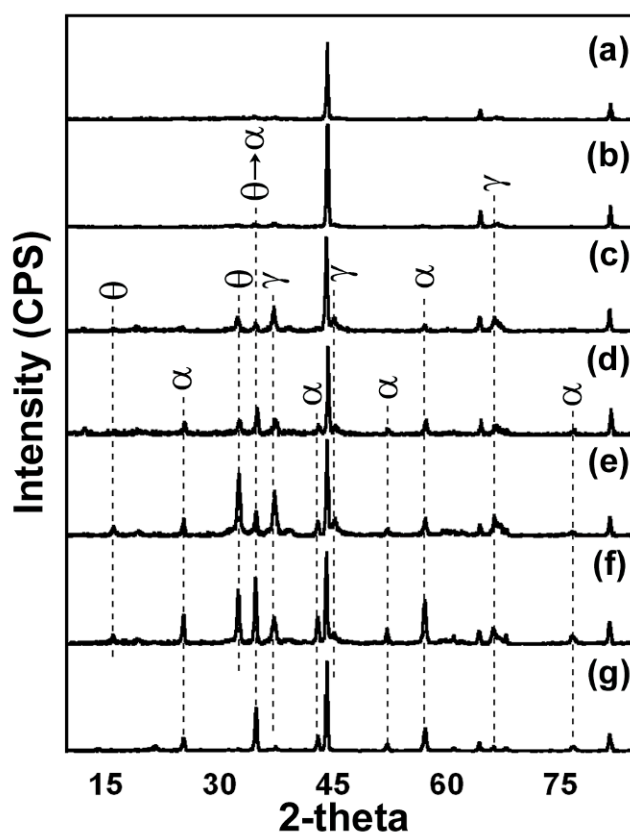


Figure 6.3. XRD profile for different oxidation times: (a) $t_{\text{ox}} = 0.25$ hr, (b) $t_{\text{ox}} = 1$ hr, (c) $t_{\text{ox}} = 5$ hrs, (d) $t_{\text{ox}} = 10$ hrs, (e) $t_{\text{ox}} = 24$ hrs, (f) $t_{\text{ox}} = 48$ hrs, (g) $t_{\text{ox}} = 96$ hrs. Here α is shown as the representative of Rhombohedral alumina, γ of cubic alumina and θ of monoclinic alumina.

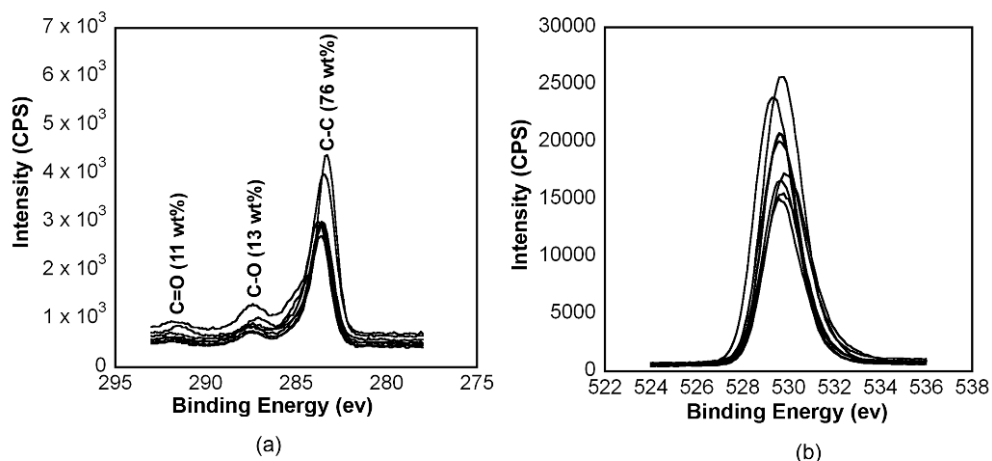


Figure 6.4. XPS plots of oxidized alloy surfaces with (a) C1s, and (b) O1s. (a) reveals that there is no distinct tendency for C contamination, and (b) reveals the absence of hydroxyl group in all specimens

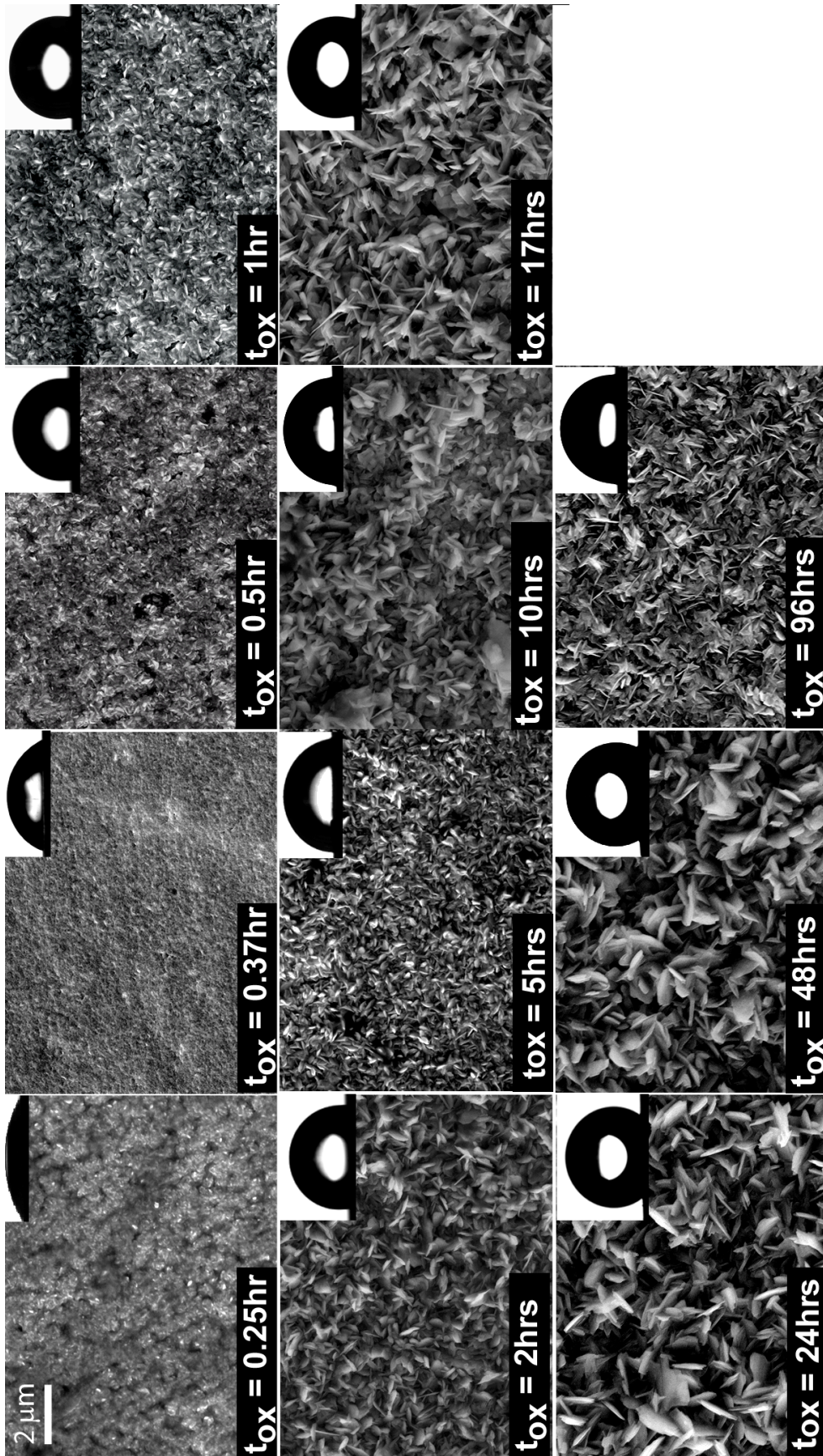


Figure 6.5. SEM images of oxidized FeCrAl surfaces for variable lengths of time. Corresponding sessile water drop image (top right) and t_{ox} values (bottom left) attached with each image. Horizontal marker bar applicable for all images showed on the top left corner.

(c) SEM

SEM, performed on all 11 samples, was recorded at the same magnification (x10000). SEM micrographs of representative specimens, presented in Figure 6.5, offer clues to interpretation of the wettability data obtained from DSA (apparent Θ results). As can be seen in the SEM images during the initial periods of oxidation when the platelets began to form and grow, contact angle increased sharply, until at $t_{ox} = 0.5$ hr, after which contact angle steadied up till $t_{ox} = 2$ hrs. However, contact angle improved drastically again after $t_{ox} = 10$ hrs until $t_{ox} = 24$ hrs. This rapid increase in contact angle may be attributed to quite well defined and evenly distributed platelets formed within this time range as revealed by the SEM micrographs. At $t_{ox} = 24$ hrs, where maximum contact angle (128°) was achieved, the microstructure appeared to have the tallest and widest platelets. After $t_{ox} = 24$ hrs contact angle decreased again possibly due to change in platelet shape hinting more γ , θ to α transformation.

(d) Quantification of morphology

In order to correlate wettability with surface morphology, image processing was carried out in the form of measuring platelet width (w), thickness (r) and interplatelet distance (d). ImageJ was used to measure the platelet dimensions according to Figure 6.6a. Figure 6.6b shows the resultant values of the platelet width as a function of oxidation time. Also in Figure 6.6c interplatelet distance and thickness values are plotted against oxidation time. Because of the randomness of the *in situ* oxide platelets that formed on the surface, standard deviation values appeared to be high in these measurements. Nevertheless, the platelet dimensions and spacing correlated well with measured apparent contact angle. It was obvious from Figure 6.6b and 6.6c that the trend of contact angle changed somewhat proportionately with width as well as interplatelet distance of the platelets.

High hydrophobicity in the presence of a Wenzel state can only be achieved if the surface is itself hydrophobic and rough. In the region of the highest hydrophobicity ($10 < t_{ox} < 48$ hours) oxide scales were found to be composed of γ , θ and α -alumina (Figure 6.3). Blonski and Garofalini [84] showed that the surface energy of α -alumina is higher than

that of γ -alumina ($2.0 - 8.4 \text{ J/m}^2$ for α -alumina and $0.8 - 2.5 \text{ J/m}^2$ for γ -alumina). This indicates that the intrinsic wetting angle of α -alumina should be lower than for γ -alumina; α should be more hydrophilic than γ .

SEM on 4 oxidized specimens that were additionally processed on one edge after oxidation (method outlined in Chapter 5) was carried out to measure the height of the oxide layer (h_{ox}). These h_{ox} values were correlated with oxidation time as shown in Figure 6.8a. It was evident from the figure that height increased parabolically with t_{ox} . However, Figure 6.7b reveals that oxide scales formed at 930°C consisted of a bilayer, with a thick and compact layer of alumina adherent to the base metal and another layer with whiskers/platelet like morphology on top of it. Upon careful observation of Figure 6.7b Platelet height (h_p) was assumed to be $1/3^{\text{rd}}$ of the height of the overall oxide height (h_{ox}) and was consequently correlated with contact angle values (Figure 6.8b).

6.1.2 Multiple stage temperature oxidation

Some polished FeCrAl strips were also oxidized in stages to achieve higher aspect ratio of platelets at a reasonably shorter time. This has been reported by Vaneman *et al.* with reasonable success from morphological standpoint [85]. Table 6.2 outlines multiple stage oxidation scheme employed here:

Table 6-2. Multiple stage oxidation schemes.

Sample	945°C	990°C	1005°C
A	1hr	1 hr	
B	1hr	3 hrs	
C		1 hr	1 hr
D		1 hr	3 hrs

SEM images of the resulting surfaces are presented in Figure 6.9. Observation suggests that samples that were allowed more growth time i.e., were kept at higher temperatures for longer periods of time produced platelets with higher aspect ratio. One obvious advantage of multiple stage oxidation was that it exhibited similar morphological attributes at a much lower total oxidation time than single stage (4 hours of staged

oxidation compared to 24 hours at 930°C). Hence multiple stage oxidation was preferred over single stage oxidation of SMF.

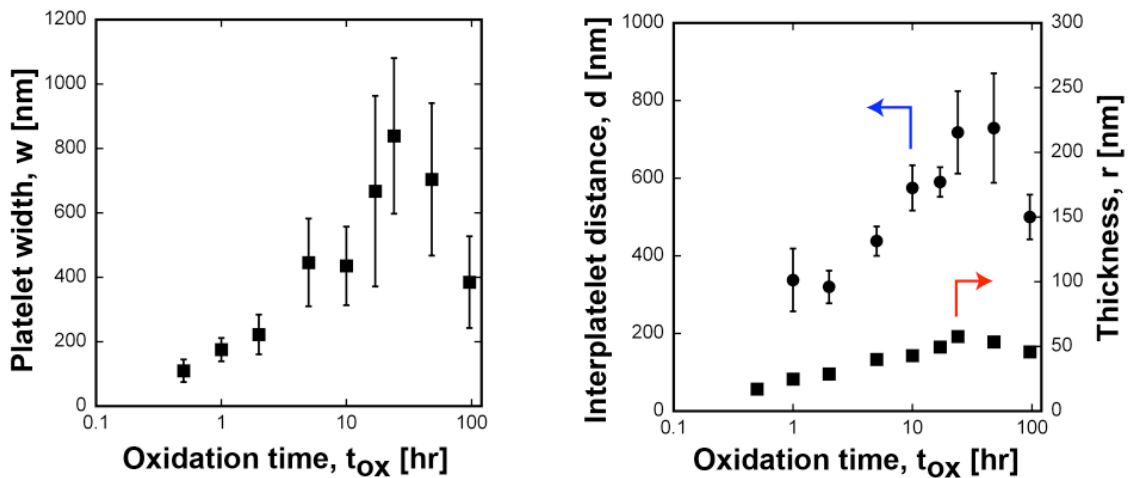
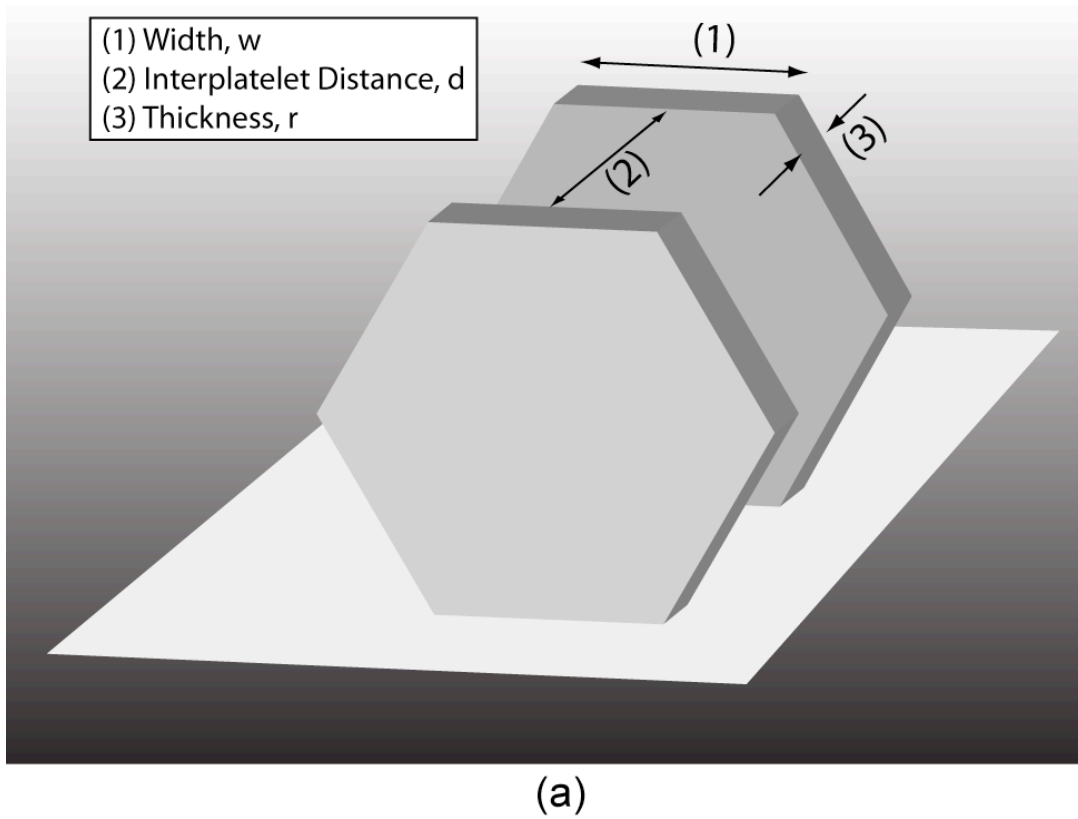
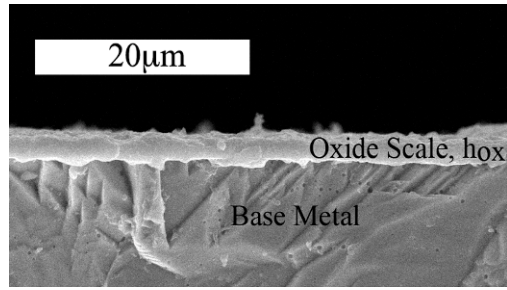
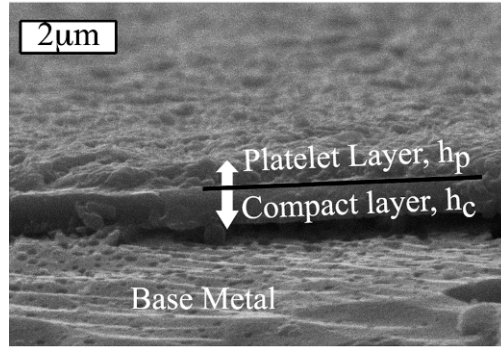


Figure 6.6. (a) Schematic of platelet width, w , interplatelet distance, d , and thickness, r , measurements, and relationship between: (b) platelet width and t_{ox} , (c) interplatelet distance, thickness and t_{ox} . Note: all measurements were taken from plan view SEM micrographs.



(a)



(b)

Figure 6.7. Measurement of scale height (h_{ox}) from etched edge of oxidized FeCrAl with (a) showing a representative cross-section; a layer of oxide scale on base metal (Oxidation condition: $T = 930^{\circ}\text{C}$ and $t_{ox} = 24$ hrs) and (b) showing evidence of bilayer oxide formation (Oxidation condition: $T = 930^{\circ}\text{C}$ and $t_{ox} = 2$ hrs) where, $h_{ox} = h_c + h_p$.

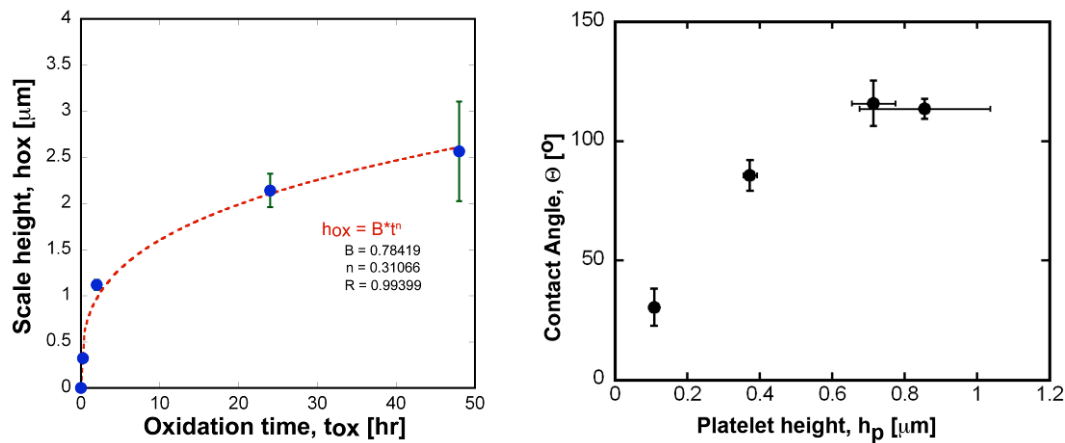


Figure 6.8. Observed correlation between: (a) scale height and t_{ox} (Inset: Equation and related parameters obtained via curve fitting) and (b) platelet height, h_{op} (taken as $1/3^{\text{rd}}$ of the overall scale height, h_{ox}) and contact angle.

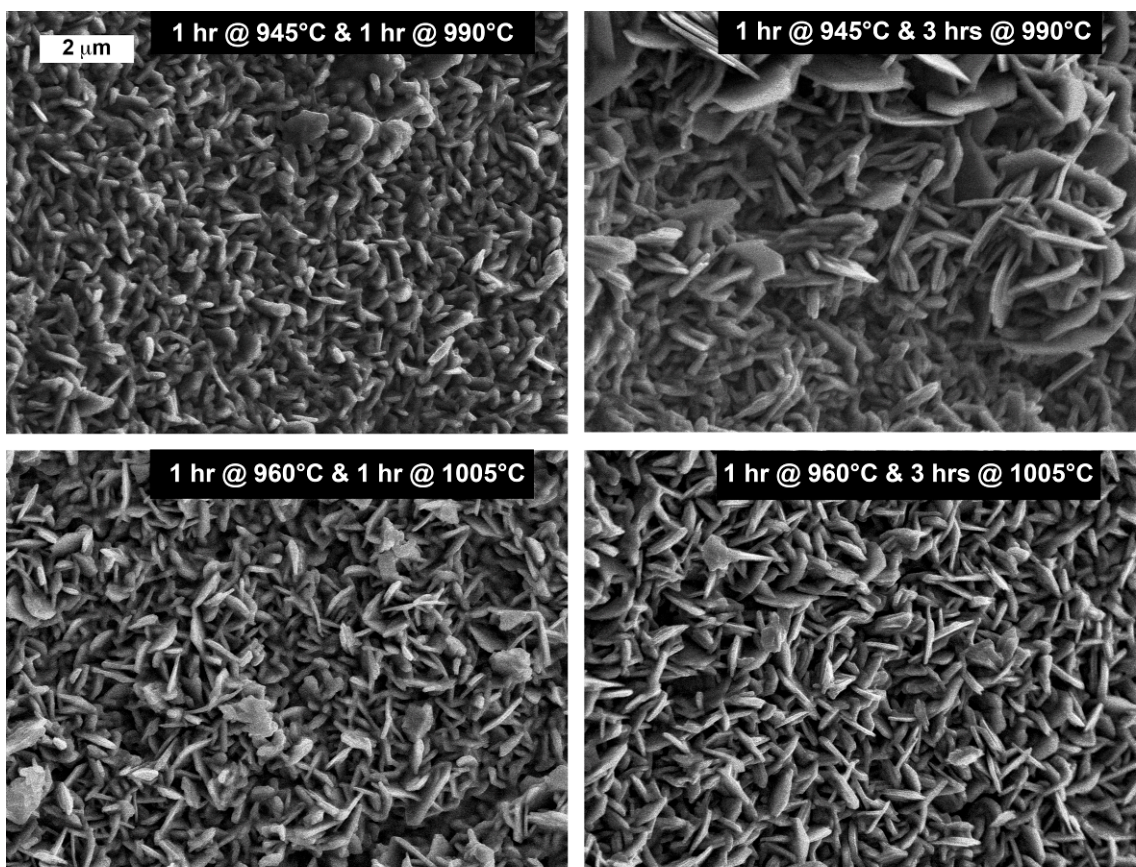


Figure 6.9. SEM micrographs of multiple stage oxidation. Inset: Operating conditions. All images have been taken at 30° tilt except the one oxidized for 1 hr at 960°C and 1 hr @ 1005°C which was taken at 0° tilt. Scale bar attached with the top left image is applicable for all images.

6.1.3 Oxidation of sintered metal fiber (SMF)

After analyzing the oxidation behavior of FeCrAl strip, attention was finally directed towards oxidizing the actual support, sintered metal fibers (SMF). Upon reviewing SEM images of the oxidized alloy strip it was decided that multiple stage temperature oxidation would be applied to SMF. SEM images of the resulting surfaces have been presented in Figure 6.10.

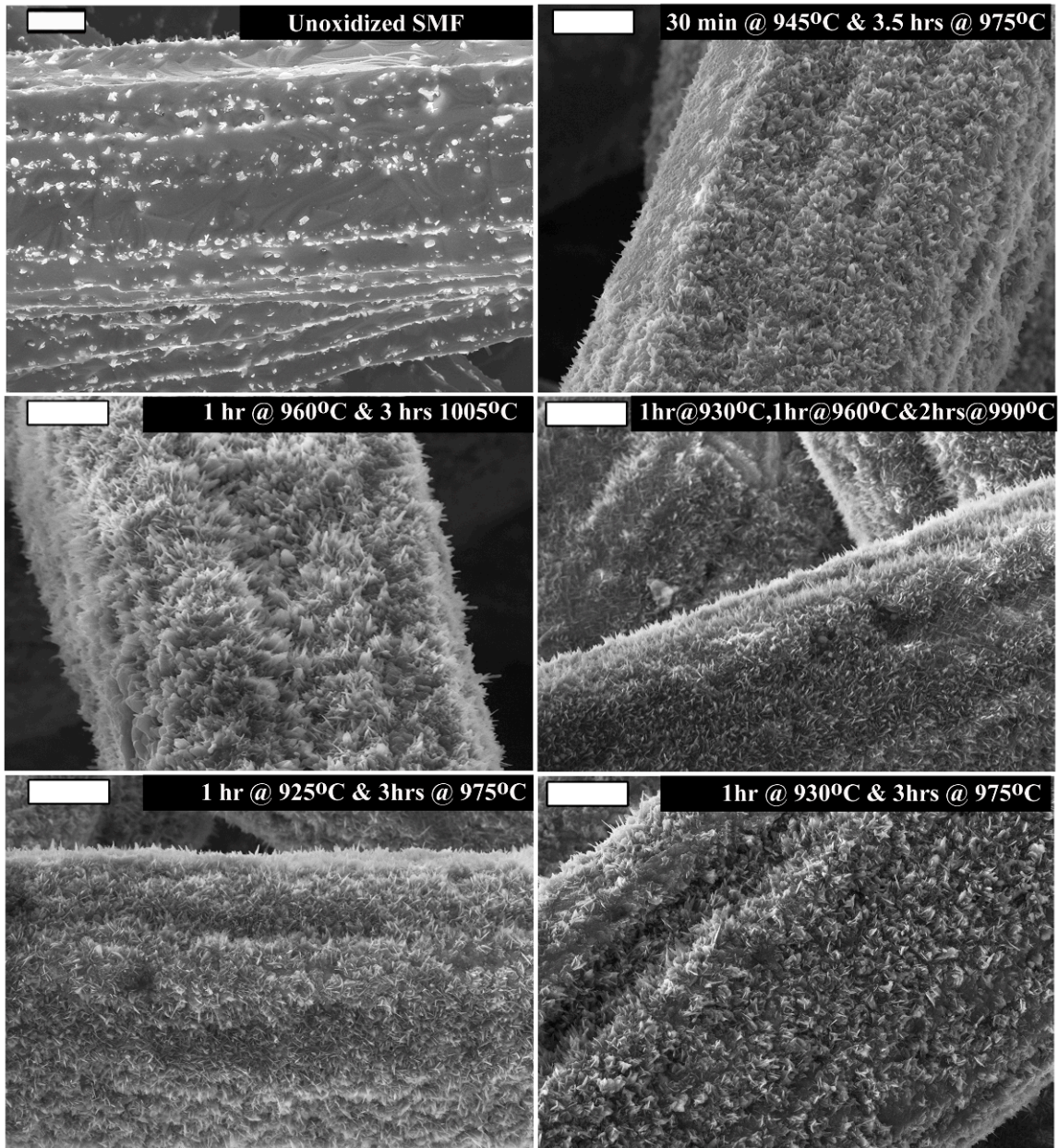


Figure 6.10. SMFs oxidized at different multiple stage temperatures. Scale bar is 20 μm. Operating condition has been attached with each image.

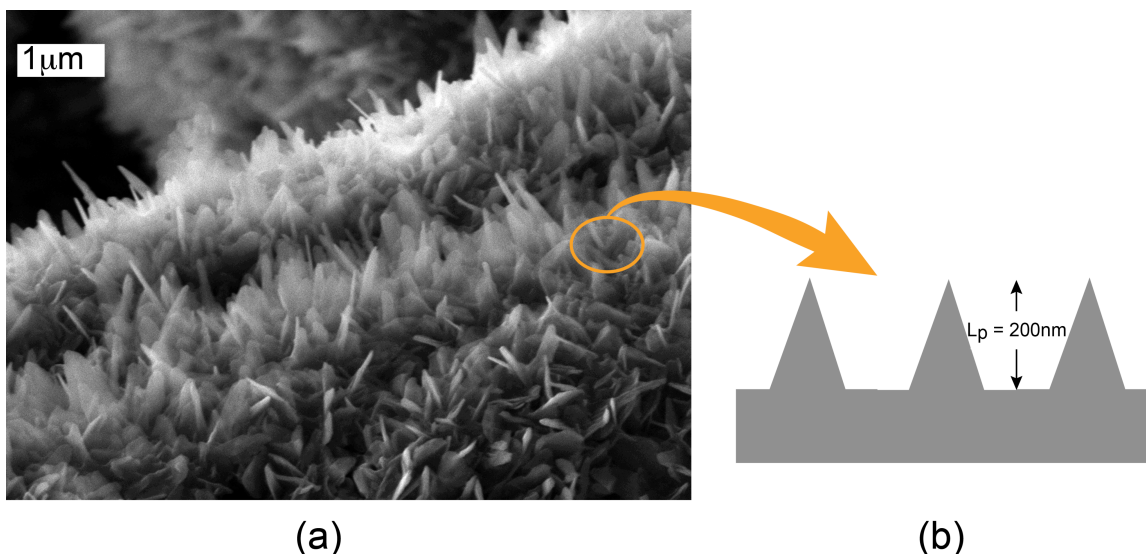


Figure 6.11. (a) Higher resolution image of catalyst support (oxidation condition: 1 hr at 930°C, 1 hr at 960°C and 2 hrs at 990°C). (b) Simple schematic of whiskers formed at (a).

6.1.3.1 Analysis of morphology of oxidized SMF

Topographic differences between the oxide scale produced on alloy strip and that on SMF were notified from Figure 6.10: the scale on the strip resembled platelets, whereas the latter resembled whiskers. Upon careful observation of the images the final support was selected to be the one that formed upon oxidation for 1 hr at 930°C, 1 hr at 960°C and 2 hrs at 990°C. Oxide scales formed on base metal SMF via this oxidation treatment have been tested in the subsequent steps and hence, from now on, will be referred to as ‘catalyst support’.

An SEM image of the catalyst support taken at higher magnification reveals (Figure 6.11a) that the oxide scale comprises of randomly oriented whiskers, quite identical to the proposed support morphology described in Chapter 1. Further analysis of morphology included measurement of BET surface area which was found to be $\sim 0.50\text{m}^2/\text{g}$ for the support. It was quite low compared to the BET surface area found for unoxidized SMF ($\sim 0.35\text{ m}^2/\text{g}$). From this comparative study of surface area it was assumed that the catalyst support formed in this case is nonporous. This assumption is used later in this Chapter to calculate Carberry number. Besides Image J was used to estimate the height of

whiskers which was found to be ~ 200 nm (202.8 ± 34.4). This value was used as the pore length (L_p) in the calculation of Wheeler-Weisz number. A simplified schematic of the morphology of whiskers is presented in Figure 6.11b.

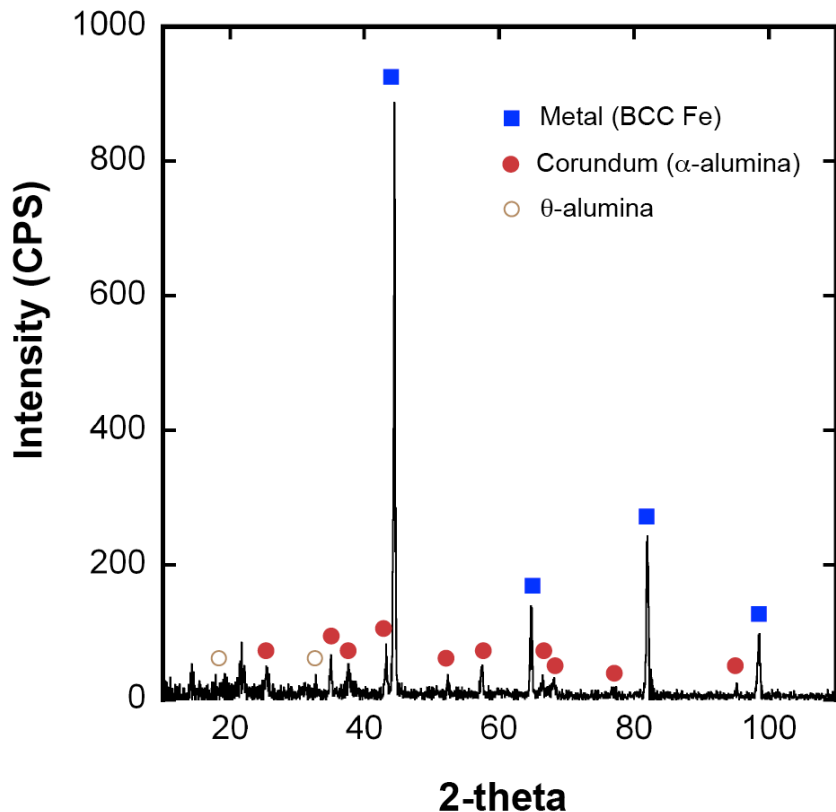


Figure 6.12. XRD profile of SMF oxidized at multiple stage (Oxidation condition: 1 hr at 930°C, 1 hr at 960°C and 2 hrs at 990°C).

6.1.3.2 Characterization of support

From the XRD profile it was revealed that the surface of oxide support was covered mostly with α -alumina (Figure 6.12). Contact angle of oxidized SMF, measured via DSA, was found to be almost similar to that of unoxidized SMF (Figure 6.13). Structurewise SMF consists of fibers intertwined together to form mesh that already has significantly large number of air pockets ($\epsilon = 0.8$). These air pockets might have raised the contact angle via establishment of Cassie-Baxter state. Overwhelming influence of these macro air pockets might have negated the effect of whatever morphological change individual fiber had gone through upon oxidation. This argument justifies unchanged

contact angle observation. From the DSA results it can be speculated that the likelihood of having trapped air might hinder proper wetting of support. However, this dewetting mode seemed to be unstable since alumina is intrinsically hydrophilic. Hence wetting can be achieved on those surfaces if trapped air bubble escapes with the application of extra force (possibly via ultrasonic treatment).

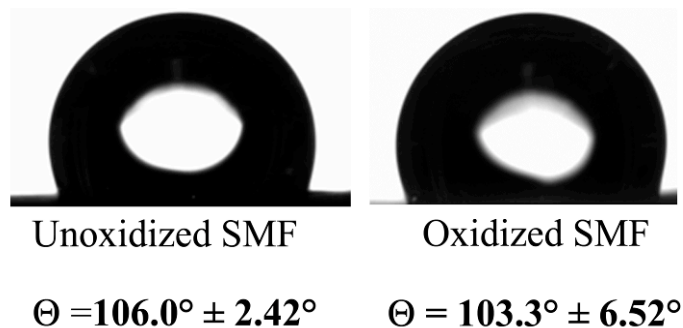


Figure 6.13. DSA images water drops and contact angle values of oxidized and unoxidized SMF.

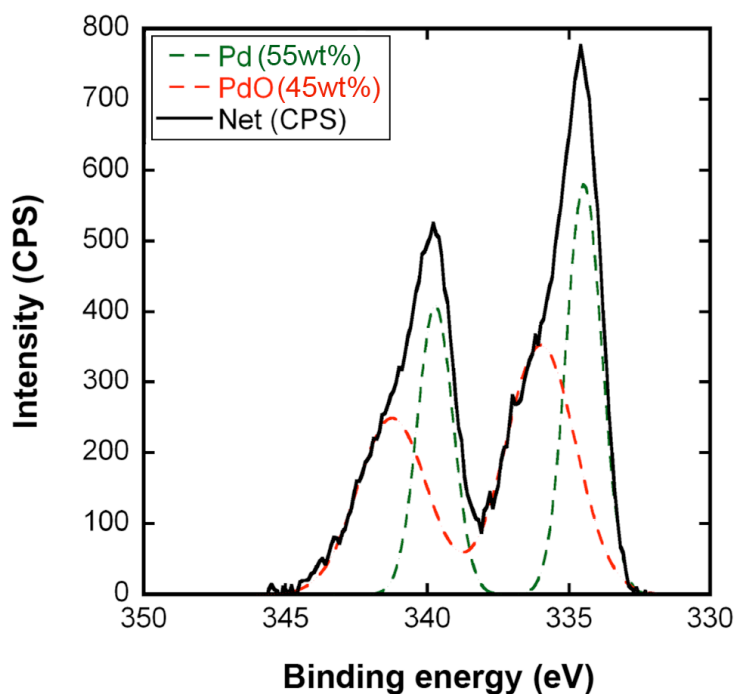


Figure 6.14. High resolution XPS spectrum of Pd 3d. Inset: different forms of Pd and their atomic percentages (Cl was found in survey plot with composition of $\sim 1.7\text{wt}\%$ compared to $\sim 4.6\text{wt}\%$ Pd).

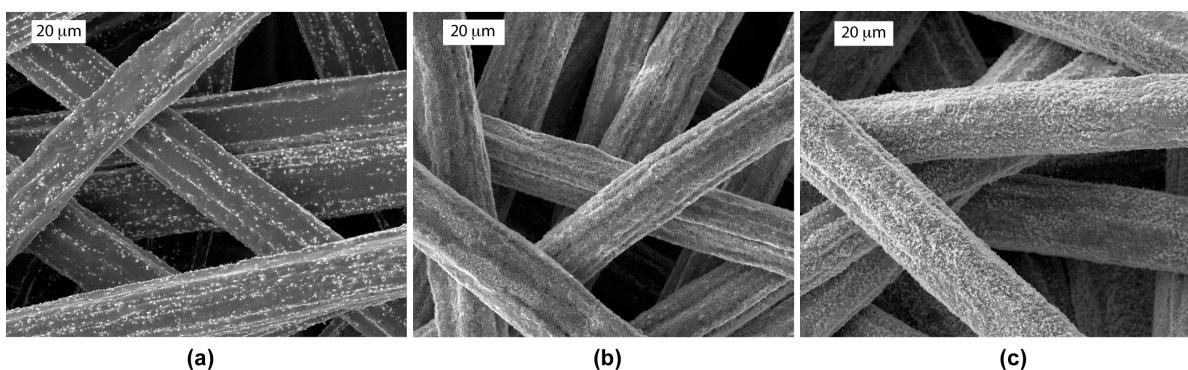


Figure 6.15. SEM microphotographs of (a) bare SMF, (b) oxidized SMF and (c) oxidized SMF after Pd deposition.

6.1.3.3 Characterization of Pd/SMF

Pd was deposited on support via incipient wetness impregnation (method outlined in Chapter 5). After deposition the support was reduced for desired particle size of Pd. The appearance of the specimens upon reduction was darker which is diagnostic of their reduced state. High resolution XPS profile of the reduced support revealed the presence of Pd in both metallic as well as oxide form (PdO). Figure 6.14 shows Pd 3d peaks obtained from XPS.

SEM microphotographs of oxidized SMF before and after Pd deposition are presented in Figure 6.15. The microfibers of SMF, fully coated with oxide platelets are further covered with Pd after deposition. Coating of SMF with a catalytically active thin layer facilitates high permeability and low pressure drop during fluid passage.

6.1.3.4 Mechanical and Chemical Stability of support

Mechanical stability of the oxide support was tested using ultrasonic adherence test. Cavitation bubbles collapse close to a solid boundary and the damage by these bubbles is caused by shock waves. The attained maximum impulsive pressure and gas temperature at the bubble center are 2265 atm and 4151K respectively [95]. After 40 minutes of ultrasonic treatment SMF mass remained almost unchanged ($\leq 0.2\%$ decrease). On the other hand, in order to analyze chemical stability, the support was immersed into an acid

mixture of 1:1:1 HCl, HNO₃ and H₂O (detail outlined in Chapter 5). Figure 6.16 displays negligible mass loss of oxide support with immersion time. The mass loss profile for unoxidized SMF has also been reported in Figure 6.16, showing that oxidized SMF possesses much improved chemical stability in strong acid. Whereas unoxidized SMF completely dissolves in acid within 15 minutes, oxidized SMF was able to retain more than 90% of its original mass after 80 minutes of immersion. Moreover, most of the mass loss occurred during handling with tweezers. Using tweezers as a clamp to keep entire SMF surface exposed to acid during immersion might have facilitated stress corrosion at the point of its attachment with the specimen. Observation of maximum mass loss occurring at the point of attachment justifies this argument. Extensive acid stability of oxidized SMF was due to the formation of protective oxide scale on the base metal surface.

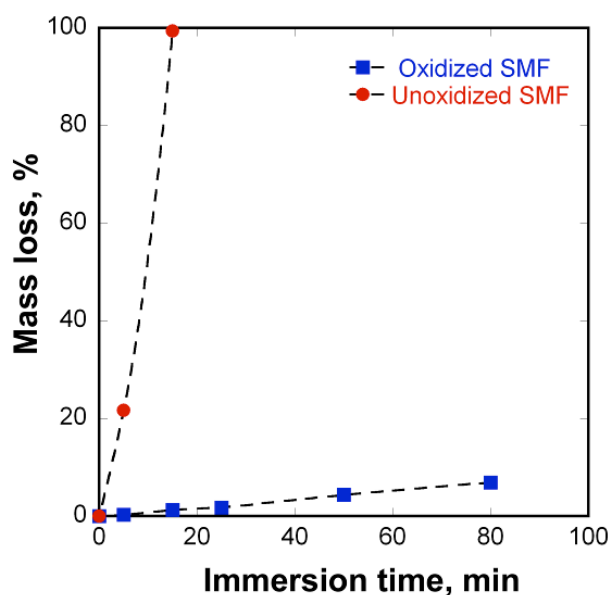


Figure 6.16. Mass loss profile upon immersion in acid for both oxidized and unoxidized specimens.

6.2 Three phase hydrogenation reaction

Two reaction schemes have been addressed in this study (Figure 6.17). Reaction scheme 1 is regarded as a model reaction for carbon-carbon double bond hydrogenation happening during oil upgrading. The reaction scheme 2 allows selectivity study in hydrogenations. The developed Pd/SMF catalyst is supposed to provide kinetic regime in

three-phase hydrogenations, which are widely known for mass transfer limitations [86]. Heat transfer limitations are usually out of concern in liquid phase, and for Pd-catalyzed MBY hydrogenation were shown to be absent: previous reports prove negligible temperature rise occurs in between bulk liquid and catalyst surface [87]. Hence the reaction can be said to be operating under isothermal conditions.

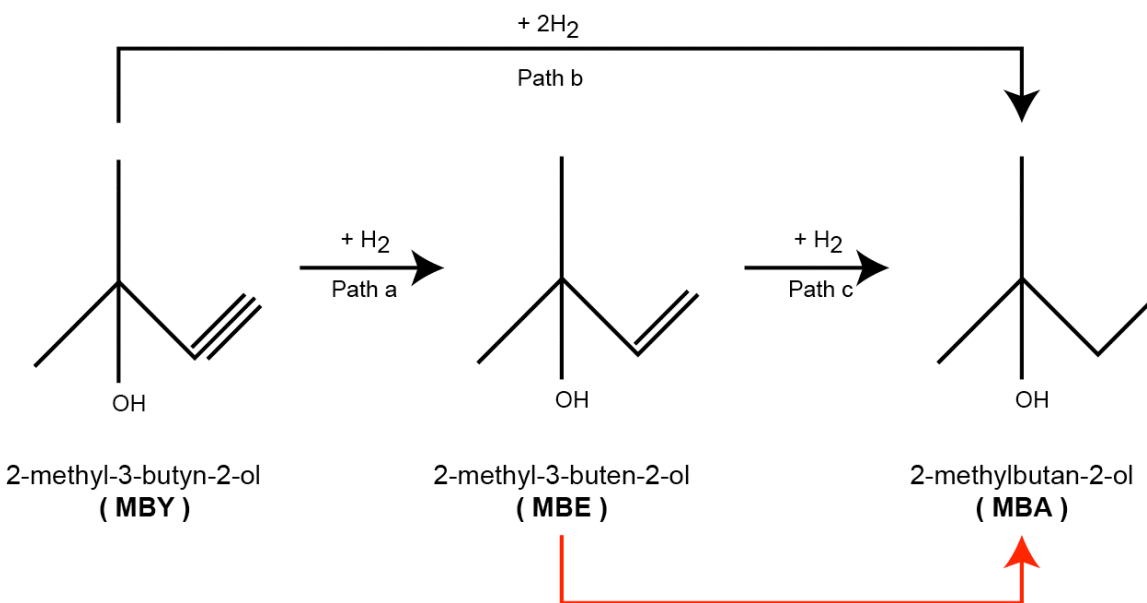


Figure 6.17. Three phase hydrogenation reaction schemes. Red arrow indicates reaction path for scheme 1 and black arrow (path a,b,c) indicates reaction paths for scheme 2.

Catalytic activity of the reactor was observed during preliminary blank runs using reaction scheme 1. In order to check for ‘wall effects’ subsequent reactions were run with and without catalyst but at the same reaction condition (40°C, 0.46 MPa H₂, 0.04M MBE and 1200 rpm stirring speed) and their slope values obtained from pressure drop in gas burette were compared. Slopes were found to be 2.8x10⁻⁵ (without a catalyst), 2.2x10⁻⁴ (with the catalyst with 0.53 Pd wt% loading), and 1.1x10⁻⁴ (with the catalyst with 0.29 Pd wt% loading). Results suggested that ‘wall effect’ could not be disregarded as the slope value obtained without catalyst was more than 10% of that obtained with catalysts. In order to address this wall effect, observed slope value from individual run had been reduced by 12.7% to determine the actual reaction rate for the catalyst with 0.53 wt% Pd loading, and by 25% for the catalyst with 0.29 Pd wt% loading. For the activation energy

estimation, only the catalyst with higher loading was used to prevent the influence of the wall activity.

6.2.1 MBE hydrogenation

Absence of external gas-liquid mass transfer limitations in MBE hydrogenation was examined by running several reactions at the same conditions but for different stirring speeds (600 rpm, 1000 rpm and 1200 rpm) (Figure 6.18). The reaction rate curve became quite asymptotic in the region between 1000 and 1200 rpm suggesting that in this region the reaction is not be affected by external mass transfer limitation.

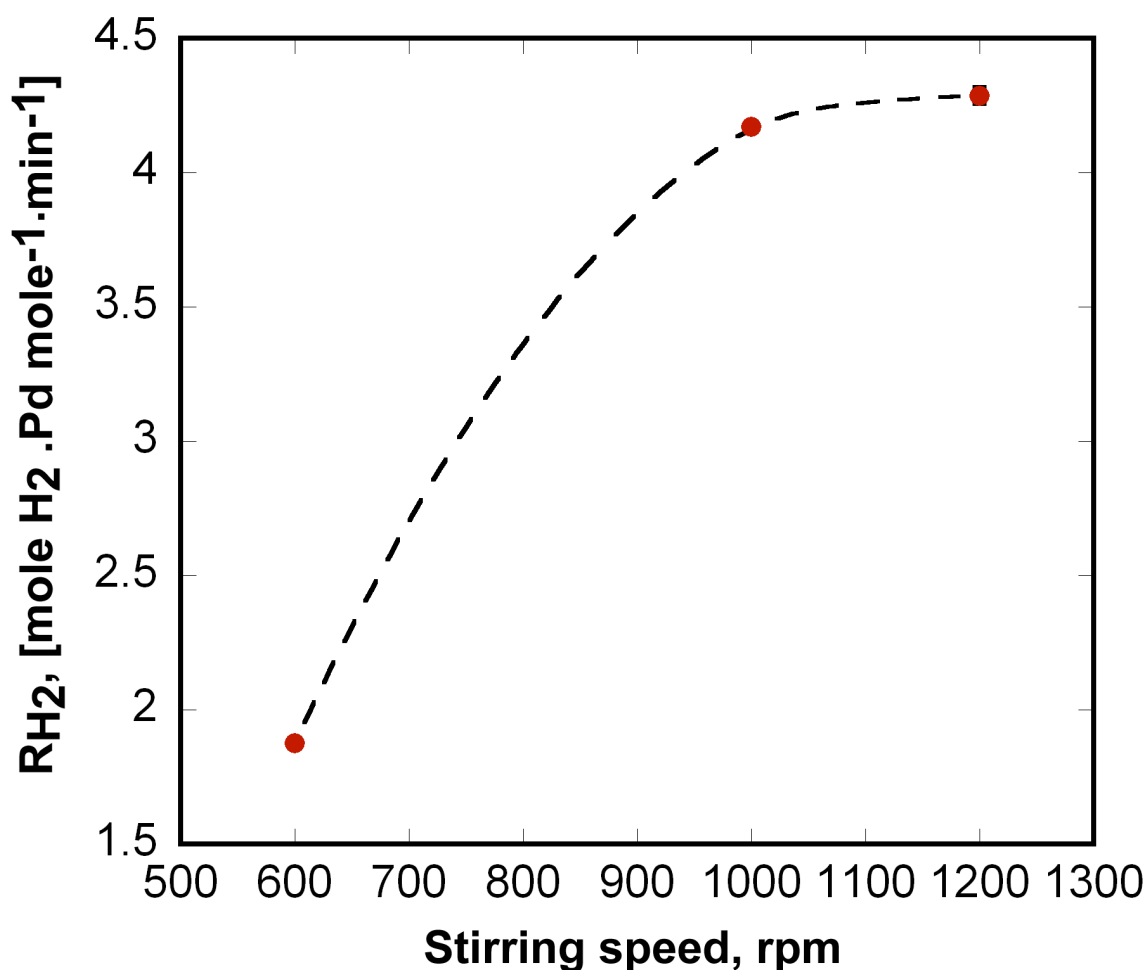


Figure 6.18. Change in reaction rate with stirring speed. Reaction conditions: 50°C, 0.46 MPa H₂, 0.12 mg Pd (calculated from AAS).

A Madon-Boudart test was performed in MBE hydrogenation. It tests the absence of all mass transfer limitations, including external gas-liquid, liquid-solid and internal ones [90]. Two different Pd loadings (0.29 wt% and 0.53 wt%) were tested under the same conditions (40°C, 0.46 MPa H₂, 0.13 mg Pd). Rate values were found to be 3.0 ± 0.3 mole H₂.Pd mole⁻¹.min⁻¹, indicating that the reaction occurs in a kinetic regime under the condition of the same Pd particle size.

A Wheeler-Weisz group (Eq 2-7) is another criterion, which allows estimation internal mass transfer limitations in the absence of external ones:

$$WW = L_p^2 \times \frac{R \times \rho_s}{D_{eff} \times C_l} \quad (2-7)$$

$$D_{eff} = D_i \times \frac{\varepsilon}{\tau} \quad (6-1)$$

where D_{eff} is the effective diffusion coefficient inside the catalyst pores, D_i is a diffusion coefficient of either hydrogen or MBE in ethanol, ε is the porosity, 0.8 (from Chapter 6) and τ is the tortuosity of the catalyst. Usually, for alumina it is assumed to be 4, but in the current study the pores are straight between the alumina whiskers, so the tortuosity factor is assumed as 1. This again shows the advantage of the developed support: the reactant effective diffusivity can be 4-fold as high as in conventional alumina supports, providing excellent mass transfer within the pores.

Length of the pores in equation (L_p) in Eq 2-7 was assumed to be equal to the height of oxide whiskers (200 nm). The molecular diffusivities of hydrogen, MBE and MBY in ethanol at 40°C were taken as 3.1×10⁻⁹ m²/s (H₂), 1.1×10⁻⁹ m²/s (MBE) and 1.1 × 10⁻⁹ m²/s (MBY) [88].

The Wheeler-Weisz group values for MBE and hydrogen were found as 0.0027 (H₂) and 0.003 (MBE), confirming the absence of internal diffusion limitations (WW < 0.1). Note, that with the traditional alumina support this value can be ~4 times higher due to the tortuosity factor of 4, i.e., more susceptible to internal diffusion limitations.

The effect of temperature on the hydrogenation of MBE (Reaction scheme 1) was studied in the kinetic regime with 5 different temperatures within the temperature range of 35 to 50°C. From the Arrhenius plot (Figure 6.19) of the observed data, the apparent activation energy was found to be 32.6 ± 2.4 kJ/mol (Standard deviation value found using LINEST function in MS Excel). Relatively high value (more than 5-15 kJ/mole) of activation energy again proves the absence of external mass transfer limitations.

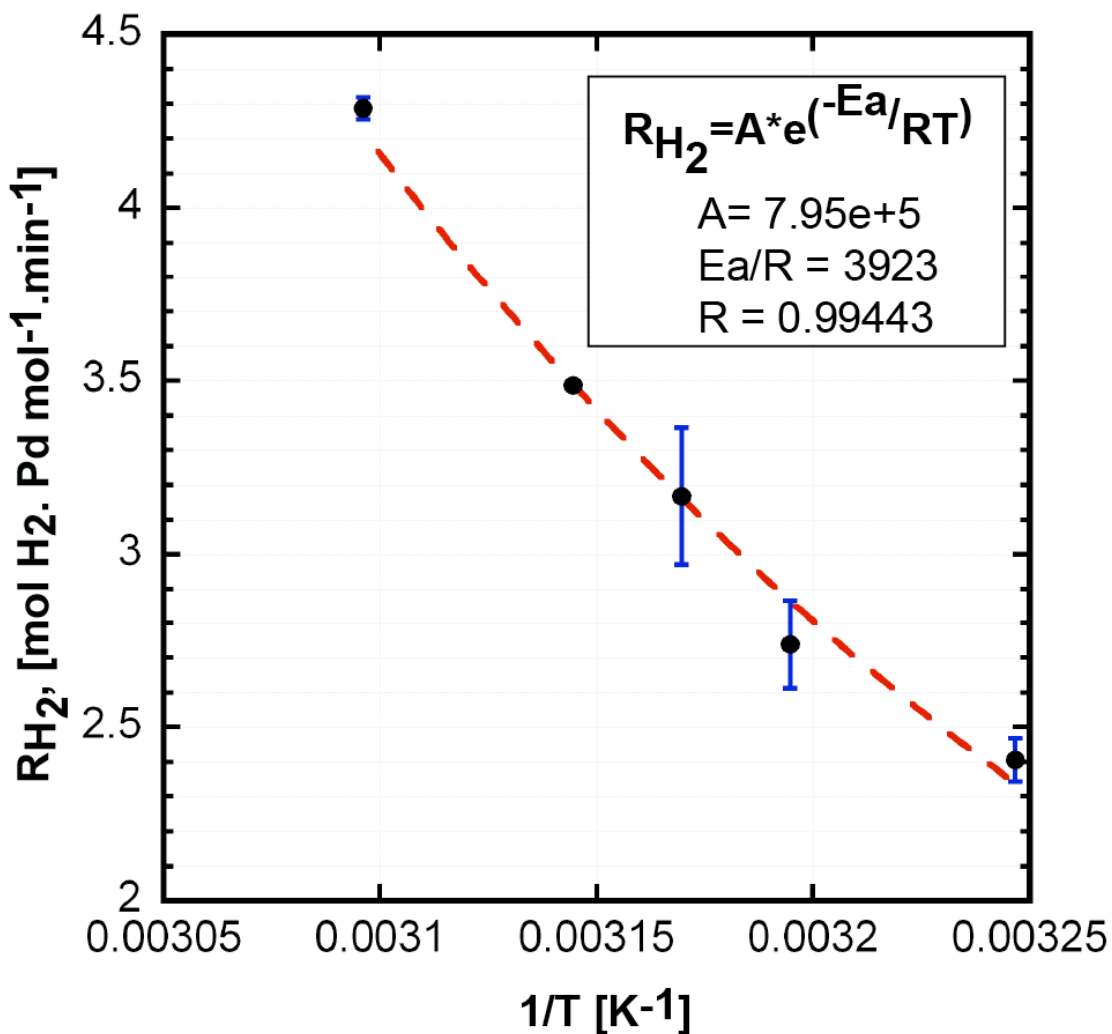


Figure 6.19. Arrhenius plot constructed for the temperature range of 35° - 50°C. Reaction conditions: 0.46 MPa H₂, 0.14 mg ± 0.04 Pd (calculated mass from AAS).

Thus, the SMF support prevents the influence of mass transfer limitations in C-C double bond hydrogenations, frequently taking place in oil upgrading. It is important that Pd is the most active metal for this reaction (more active than Ni used in oil hydrotreating), so the appearance of mass transfer limitations in Ni-catalyzed reactions is even less likely than in Pd-catalyzed reaction. This proves that the developed support is an excellent candidate to provide kinetic regime in three-phase hydrogenations of carbon-carbon double bonds (C=C), which complements its high mechanical and chemical stability discussed above.

6.2.2 MBY hydrogenation

Three-phase hydrogenations are also widely used in fine chemical industry in selective triple C-C bond hydrogenations to double C-C bond. In the present study, a possibility of the catalyst use in MBY hydrogenation to MBE was evaluated as well.

Figures 6.20 and 6.21 show reaction mixture composition vs. time profiles and selectivity vs. MBY conversion, respectively, during MBY hydrogenation at 1200 rpm, 0.46 MPa hydrogen, initial MBY concentration of 0.04M and initial MBY-to-Pd molar ratio as 10^4 mol(MBY)/mol(Pd). Appearance of MBA at very early stages of reaction supports the presence of an active parallel path (path b in Figure 5.4 Chapter 5) of MBY hydrogenation where MBY directly converts to MBA. This occurrence of direct alkane formation may be because of multiple bound ethylidyne species [91]. Selectivity of MBE to MBA with respect to molar conversion of MBY has been plotted in Figure 6.21 which shows that selectivity decreases at higher MBY conversion, when MBE concentration becomes higher and MBE competes with MBY for active sites.

The reaction rate of MBY hydrogenation was found to be two orders of magnitude higher than that of MBE hydrogenation (Table 6-3), making this reaction highly susceptible to mass transfer limitations. Previously, MBY external liquid-solid mass transfer was found to be rate limiting with industrial powdered catalyst [14]. Carberry number (Eq 2-4) was

estimated in the current study to verify if the MBY mass transfer limits the reaction with the arranged catalyst.

Carberry number compares the observed reaction rate with maximum reaction rate i.e., reaction rate when concentration of the reactant at the surface of catalyst is zero. A Carberry number (Ca) value less than 0.05 would indicate absence of mass transfer limitation. In the studied reaction hydrogen was present at low concentration over the entire reaction range. Therefore, hydrogen can be regarded as limiting reactant at initial stages. Other reactants (MBY or MBE) can also become limiting at the end of the reaction. Nevertheless, Carberry number was estimated for both hydrogen and the other reactant(s) both at the initial stage and near the end (peak). Both reaction schemes (1 & 2) were addressed in this purpose.

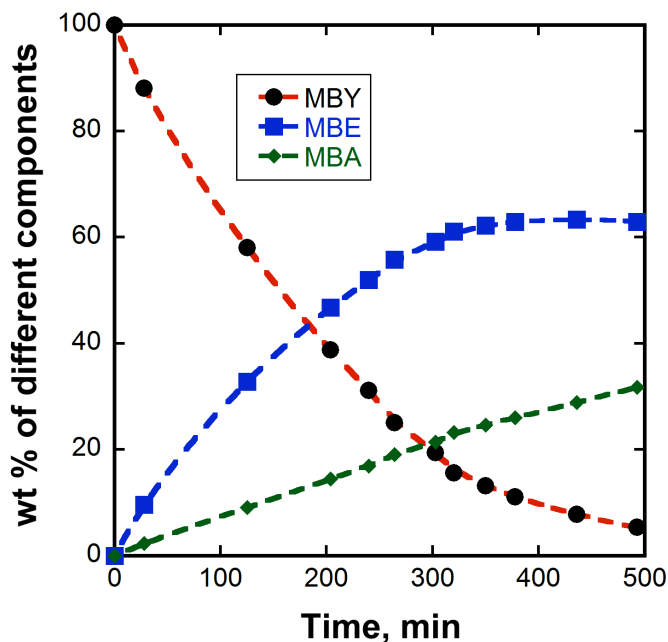


Figure 6.20. Kinetics curves of MBY hydrogenation. Reaction conditions: 40°C, 1200 rpm stirring speed, 0.46 MPa H₂ pressure, 0.09 mg Pd (calculated mass from AAS).

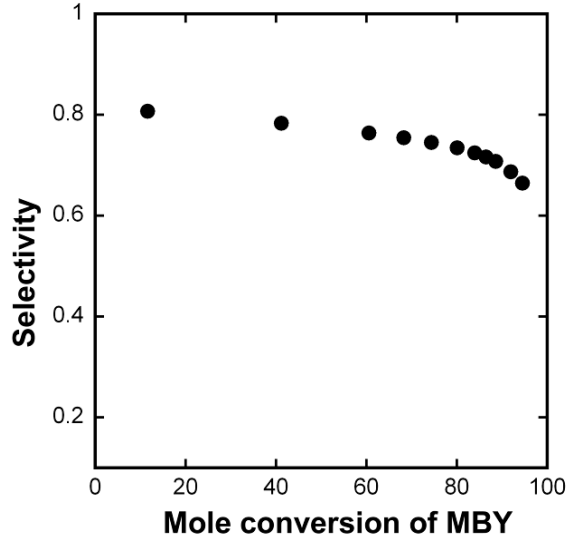


Figure 6.21. Selectivity to MBE vs. MBY conversion

Determination of Carberry number requires estimation of mass transfer coefficients for individual reactant. This was performed by using Sherwood-Frössling correlation for slurry system with gas bubbles [93] (Eq 6-2).

$$Sh = 2 + 0.4 \times \left(\frac{N \times l^5 \times n^3 \times \rho^3}{V_L \times \mu^3} \right)^{0.25} \times d_p \times (Sc)^{0.33} \quad (6-2)$$

where, Sc is the Schimidt number (Eq 6-3).

$$Sc = \frac{\mu}{\rho \times D_{1,2}} \quad (6-3)$$

Here μ and ρ are the viscosity and density of the solvent (ethanol) respectively. $D_{1,2}$ denotes the diffusivity of 1 in 2. The diffusivities of hydrogen and MBE in ethanol were found above. The diffusivity of MBY was assumed to be the same as the one of MBE.

Sc values (Eq 6-3) for H₂, MBE and MBY were found to be 344, 971 and 971 respectively. Higher Sc values for MBE and MBY suggest that their diffusion is much slower than H₂. This is due to their larger molecular size compared to small hydrogen molecules.

Of the other parameters in Sherwood number calculation (Eq 6-2), N is a power number estimated as 8.5 [92] for this system; l is impeller diameter, 0.03 m; n is angular velocity for impeller, 125.67 rad/s; ρ is ethanol density, 772 kg/m³ [89]; V_L is liquid volume, 0.2 x10⁻³ m³. Finally, d_p is the catalyst particle diameter. Since for the studied system the catalyst was not spherical, the value of d_p was assumed to be equal to equivalent diameter obtained from Eq 6-4.

$$d_p = \frac{6}{a_s \times \rho_s} \quad (6-4)$$

In this equation a_s is the external surface area of catalysts and ρ_s is the density of support (alumina), 4 g/cm³. External surface area value was assumed to be equal to the BET surface area of nonoxidized SMF i.e., 0.35 m²/g. This assumption was made because of the nonporous nature of the support. Using these values the Sherwood numbers (Sh) were found to be 4 and 5 for H₂ and MBE/MBY respectively. Finally in order to calculate Carberry number (Eq 2-4) liquid-solid mass transfer coefficient (k_{ls}) was calculated from Eq 6-5.

$$Ca = \frac{R_{obs}}{R_{max}} = \frac{R}{k_s a_s C_{H_2, liq}} \quad (2-4)$$

$$k_{ls} = \frac{Sh \times D_{1,2}}{d_p} \quad (6-5)$$

From Eq 6-5 k_{ls} values were found to be 3 x 10⁻³ m/s and 1 x 10⁻³ m/s for H₂ and MBE/MBY respectively.

Finally the Carberry numbers estimated using Eq 2-4 for two reactions schemes at both initial and final stage are presented in Table 6-3 along with other underlining parameters. In that equation (Eq 2-4) the liquid-solid mass transfer limitation can be neglected if $Ca \leq 0.05$. It should be noted that Carberry number estimation via Sherwood number calculation (Eq 6-2) results in a standard deviation of 30% [93].

From the data presented in Table 6-3 it can be summarized that for reaction scheme 1 mass transfer limitation can be safely neglected. For reaction scheme 2, mass transfer of either of the reactants during the initial stages (12% conversion) is not limiting. Near the end of the reaction (88% conversion) mass transfer of MBY seems to be limiting which is quite common during this stage of reaction [14].

Table 6-3. Results obtained from the calculation of Carberry number

RS*	Bulk concentration, C_b mol/m ³	Initial values		Peak values		Carberry number, Ca
		C, mol/m ³	Reaction Rate, mol kgcat ⁻¹ s ⁻¹ X 10 ⁻³	C, mol/m ³	Reaction Rate, mol kgcat ⁻¹ s ⁻¹ x 10 ⁻³	
1	16 (H ₂)	40 (MBE)	2.2 ± 0.1 (H ₂) 2.2±0.1 (MBE)	-	-	0.00012 (H ₂) 0.00011 (MBE)
2	16 (H ₂)	35.82 (MBY) (after 28 min)	676 (H ₂) 567 (MBY)	5.33 (MBY) (after 350min)	289 426	Peak: 0.02(H ₂), 0.11 (MBY) Initial: 0.04 (H ₂), 0.024 (MBY)

*RS = Reaction Scheme number

Thus, the structured catalyst is also active in triple C-C bond selective hydrogenations, and the initial reaction period is not influenced by mass transfer limitations, while the reaction becomes mass transfer limited at the reaction peak. Note, that the MBY concentration used in this study is very low as compared to the industrial solvent-free process, so that the industrial reaction conditions are less likely to cause mass transfer limitations. The study shows a possibility of the arranged catalyst application in MBY hydrogenation, and more detailed studies are necessary to evaluate reaction kinetics.

Chapter 7

Conclusions

A new catalyst support having open pore structures, much different from the conventional types has been fabricated via thermal oxidation and tested with a representative three phase catalytic reaction in a semibatch reactor. The surface of the support was characterized in order to evaluate different underlying physical and chemical properties. The results can be summarized as follows:

1) Multiple stage temperature oxidation was found to be an advantageous fabrication method for the oxide support compared with isothermal oxidation.

- Multiple stage temperature oxidation produced desired morphological features at a much shorter time than single isothermal stage operations (4 hours compared to 24 hours). This was probably due to separate assigned temperatures to enhance nucleation and growth rate.
- Oxidation product formed after 1 hour at 930°C, 1 hour at 960°C and 2 hours at 990°C has been selected as catalyst support.

2) Surface characterization of oxide supports was performed first on FeCrAl strips (Kanthal A1) and later carried on to SMF. The following results were obtained:

- Wettability of isothermally oxidized alumina for different lengths of time revealed that despite alumina being intrinsically hydrophilic (contact angle $\sim 40^\circ$) it can generate a very hydrophobic surface (contact Angle $\sim 128^\circ$) during oxidation via morphological changes. However, this reduced wettability state was metastable, formed via trapped air pockets (Cassie-Baxter mode). Considerable wetting of these surfaces was achieved by destroying most of the air bubbles trapped at the solid-liquid interface.
- For isothermal oxidation the oxide surface was able to retain a considerably proportion of metastable alumina. However, for multiple stage oxidation

treatments stable α -alumina predominantly formed with little or no trace of metastable alumina.

- XRD analysis revealed that transition Al_2O_3 (θ, γ) formed at the initial stages of oxidation which transformed to stable α -alumina at higher oxidation times (t_{ox}).
- SEM micrographs revealed the morphology of the oxide support to be platelet/whisker like even when stable α -alumina is predominantly present on the surface. However, presence of oxide bilayer clearly shows that this platelet/whisker containing layer is formed atop a compact oxide layer.

3) Oxidized SMF with deposited Pd was tested in a semibatch reactor using a representative hydrogenation reaction.

- Reaction rate of MBE hydrogenation was found to be free from mass transfer limitation at 35-50°C with 1200 rpm stirring speed and 0.46 MPa hydrogen.
- Activation energy of MBE hydrogenation was found as 32.6 kJ/mol.
- The catalyst can also be used in alkyne hydrogenation with initial selectivity of 80%.

Chapter 8

Future work

This project is just the beginning of a very long journey. For three phase hydrogenation Ni-Mo is commonly used in the industry. Hence, a reaction system using Ni-Mo, instead of Pd, on the developed support will be called upon for comparison of data (hydrogen consumption, activity) between the conventional and proposed system. Catalyst lifetime will also be tested. Stability of the support at the decoking temperature (600°C) will be addressed. After laboratory testing in a batch reactor, testing in continuous reactor should be performed.

Bibliography

- [1] Rase, H. F. (2000). *Handbook of commercial catalysts: heterogeneous catalysts*, Boca Raton Florida: CRC Press.
- [2] Rochefort, A., Andzelm, J., Russo, N., and Salahub, D. R. (1990). "Chemisorption and diffusion of atomic hydrogen in and on cluster models of palladium, rhodium and bimetallic palladium tin, rhodium tin, and rhodium zinc catalysts." *Journal of the American Chemical Society*, 112(23), 8239-8247.
- [3] Speight, J. G. (2000). *The Desulfurization of Heavy Oils and Residua*, Marcel Dekker Inc., New York.
- [4] Toebes, M. L., van Dillen, J. A., and de Jong, Y. P. (2001). "Synthesis of supported palladium catalysts." *Journal of Molecular Catalysis A : Chemical*, 173(1-2), 75-98.
- [5] Somasundaran P., (2006). Editor, *Encyclopedia of Surface and Colloid Science*, Taylor & Francis, New York.
- [6] Moulijn, A. C. a. J. A. (2006). Editors, *Structured Catalysts and Reactors*. Taylor and Francis group LLC.
- [7] Sivaraj, C., Contescu, C., and Schwarz, J. A. (1991). "Effect of Calcination temperature of alumina on the adsorption impregnation of Pd (II) compounds." *Journal of Catalysis*, 132(2), 422-431.
- [8] Vergunst, T., Kapteijn, F., and Moulijn, J. A. (2001). "Monolithic catalysts - non-uniform active phase distribution by impregnation." *Applied Catalysis A: General*, 213(2), 179-187.
- [9] Marceau, E., Che, M., Čejka, J., and Zukal, A. (2010). "Nickel(II) Nitrate vs. Acetate: Influence of the Precursor on the Structure and Reducibility of Ni/MCM-41 and Ni/Al-MCM-41 Catalysts." *ChemCatChem*, 2(4), 413-422.
- [10] Martínez, A., López, C., Márquez, F., and Díaz, I. (2003). "Fischer-Tropsch synthesis of hydrocarbons over mesoporous Co/SBA-15 catalysts: the influence of metal loading, cobalt precursor, and promoters." *Journal of Catalysis*, 220(2), 486-499.
- [11] Perego, C., and Villa, P. (1997). "Catalyst Preparation Methods." *Catalysis Today*, 34(3-4), 281-305.
- [12] Ruta, M., Semagina, N., and Kiwi-Minsker, L. (2008). "Monodispersed Pd Nanoparticles for Acetylene Selective Hydrogenation: Particle Size and Support Effects." *The Journal of Physical Chemistry C*, 112(35), 13635-13641.
- [13] Ryndin, Y. A., Nosova, L. V., Boronin, A. I., and Chuvilin, A. L. (1988). "Effect of dispersion of supported palladium on its electronic and catalytic properties in the hydrogenation of vinylacetylene." *Applied Catalysis*, 42(1), 131-141.
- [14] Brühwiler, A. (2007). Dissertation. *Selective hydrogenation of an alkyne with Lindlar catalysts: Mass transfer, kinetic study, and catalyst characterization*, Ecole Polytechnique Federale de Lausanne, EPFL, EPFL.
- [15] Zhao, Y. J., Zhou, J., Zhang, J. G., Li, D. Y., and Wang, S. D. (2008). "Selective hydrogenation of benzene to cyclohexene on a Ru/Al₂O₃/cordierite monolithic catalyst: Effect of mass transfer on the catalytic performance." *Industrial & Engineering Chemistry Research*, 47(14), 4641-4647.

- [16] Doraiswamy, L. K. (2001). *Organic Synthesis Engineering*: Oxford University Press, Oxford.
- [17] Zhao, Y., Zhou, J., Zhang, J., and Wang, S. (2009). "Preparation and Characterization of Ru/Al₂O₃/Cordierite Monolithic Catalysts for Selective Hydrogenation of Benzene to Cyclohexene." *Catalysis Letters*, 131(3), 597-605.
- [18] Metaxas, K. C., and Papayannakos, N. G. (2008). "Studying the internal mass transfer phenomena inside a Ni/Al₂O₃ catalyst for benzene hydrogenation." *Chemical Engineering Journal*, 140(1-3), 352-357.
- [19] Ajmera, S. K., Losey, M. W., Jensen, K. F., and Schmidt, M. A. (2001). "Microfabricated packed-bed reactor for phosgene synthesis." *AIChE Journal*, 47(7), 1639-1647.
- [20] Wiley Critical Content. *Petroleum Technology*: (2007). John Wiley & Sons.
- [21] Veldsink, J. W., Bouma, M. J., Schoon, N. H., and Beenackers, A. (1997). "Heterogeneous hydrogenation of vegetable oils: A literature review." *Catalysis Reviews-Science and Engineering*, 39(3), 253-318.
- [22] Mozaffarian, D., Katan, M. B., Ascherio, A., Stampfer, M. J., and Willett, W. C. (2006). "Trans Fatty Acids and Cardiovascular Disease." *The New England Journal of Medicine*, 354(15), 1601-1613.
- [23] Belkacemi, K., and Hamoudi, S. (2009). "Low Trans and Saturated Vegetable Oil Hydrogenation over Nanostructured Pd/Silica Catalysts: Process Parameters and Mass-Transfer Features Effects." *Industrial & Engineering Chemistry Research*, 48(3), 1081-1089.
- [24] Kemache, N., Hamoudi, S., Arul, J., and Belkacemi, K. (2010). "Activity and Selectivity of Nanostructured Sulfur-Doped Pd/SBA-15 Catalyst for Vegetable Oil Hardening." *Industrial & Engineering Chemistry Research*, 49(3), 971-979.
- [25] Fu, C. M., and Schaffer, A. M. (1985). "Effect of nitrogen compounds on cracking catalysts." *Industrial & Engineering Chemistry Product Research and Development*, 24(1), 68-75.
- [26] Song, C. (2003). "An overview of new approaches to deep desulfurization for ultra-clean gasoline, diesel fuel and jet fuel." *Catalysis Today*, 86(1-4), 211-263.
- [27] Klimov, O. V., Pashigreva, A. V., Fedotov, M. A., Kochubey, D. I., Chesalov, Y. A., Bukhtiyarova, G. A., and Noskov, A. S. (2010). "Co-Mo catalysts for ultra-deep HDS of diesel fuels prepared via synthesis of bimetallic surface compounds." *Journal of Molecular Catalysis A: Chemical*, 322(1-2), 80-89.
- [28] Stitt, E. H. (2002). "Alternative multiphase reactors for fine chemicals - A world beyond stirred tanks?" *Chemical Engineering Journal*, 90(1-2), 47-60.
- [29] Nijhuis, T. A., Kreutzer, M. T., Romijn, A. C. J., Kapteijn, F., and Moulijn, J. A. (2001). "Monolithic catalysts as efficient three-phase reactors." *Chemical Engineering Science*, 56(3), 823-829.
- [30] Edvinsson Albers, R., Nyström, M., Siverström, M., Sellin, A., Dellve, A. C., Andersson, U., Herrmann, W., and Berglin, T. (2001). "Development of a monolith-based process for H₂O₂ production: from idea to large-scale implementation." *Catalysis Today*, 69(1-4), 247-252.
- [31] Kreutzer, M. T., Kapteijn, F., Moulijn, J. A., and Heiszwolf, J. J. (2005). "Multiphase monolith reactors: Chemical reaction engineering of segmented flow in microchannels." *Chemical Engineering Science*, 60(22), 5895-5916.
- [32] Soni, D. S., and Crynes, B. L. (1980). "Comparison of the hydrodesulfurization and

- hydrodenitrogenation activities of monolith alumina impregnated with Co and Mo and Nalcom 474 catalysts." *Abstracts of Papers of the American Chemical Society*, 179(MAR), 25-FUEL.
- [33] Scinta, J., and Weller, S. W. (1978). "Catalytic hydrodesulfurization and liquefaction of coal –Batch autoclave studies." *Fuel Processing Technology*, 1(4), 279-286.
- [34] Irandoust, S., and Gahne, O. (1990). "Competitive hydrodesulfurization and hydrodenitrogenation in a monolithic reactor." *Aiche Journal*, 36(5), 746-752.
- [35] Smits, H. A., Stankiewicz, A., Glasz, W. C., Fogl, T. H. A., and Moulijn, J. A. (1996). "Selective three-phase hydrogenation of unsaturated hydrocarbons in a monolithic reactor."
- [36] Hatziantoniou, V., and Andersson, B. (1984). "The segmented two-phase flow monolithic catalyst reactor. An alternative for liquid-phase hydrogenations." *Industrial & Engineering Chemistry Fundamentals*, 23(1), 82-88.
- [37] Wolffenbuttel, B. M. A., Nijhuis, T. A., Stankiewicz, A., and Moulijn, J. A. (2001). "Influence of water on fast hydrogenation reactions with monolithic and slurry catalysts." *Catalysis Today*, 69(1-4), 265-273.
- [38] Irandoust, S., and Andersson, B. (1988). "Mass transfer and liquid phase reactions in a segmented 2-phase flow monolithic catalyst reactor." *Chemical Engineering Science*, 43(8), 1983-1988.
- [39] Hatziantoniou, V., Andersson, B., and Schoon, N. H. (1986). "Mass transfer and selectivity in liquid phase hydrogenation of nitrocompounds in a monolithic catalyst reactor with segmented gas-liquid flow." *Industrial & Engineering Chemistry Process Design and Development*, 25(4), 964-970.
- [40] Roy, S., Bauer, T., Al-Dahhan, M., Lehner, P., and Turek, T. (2004). "Monoliths as multiphase reactors: A review." *Aiche Journal*, 50(11), 2918-2938.
- [41] Stankiewicz, A. (2001). "Process intensification in in-line monolithic reactor." *Chemical Engineering Science*, 56(2), 359-364.
- [42] Irandoust, S., Andersson, B., Bengtsson, E., and Siverstrom, M. (1989). "Scaling up of a monolithic catalyst reactor with 2-phase flow." *Industrial & Engineering Chemistry Research*, 28(10), 1489-1493.
- [43] Pena, M. A., Gomez, J. P., and Fierro, J. L. G. (1996). "New catalytic routes for syngas and hydrogen production." *Applied Catalysis a-General*, 144(1-2), 7-57.
- [44] Singh, D., Rezac, M. E., and Pfromm, P. H. (2010). "Partial hydrogenation of soybean oil using metal-decorated integral-asymmetric polymer membranes: Effects of morphology and membrane properties." *Journal of Membrane Science*, 348(1-2), 99-108.
- [45] Gryaznov, V. M., Ermilova, M. M., Morozova, L. S., Orekhova, N. V., Polyakova, V. P., Roshan, N. R., Savitsky, E. M., and Parfenova, N. I. (1983). "Palladium alloys as hydrogen permeable catalysts in hydrogenation and dehydrogenation reactions." *Journal of the Less-Common Metals*, 89(2), 529-535.
- [46] Semagina, N., Grasemann, M., Xanthopoulos, N., Renken, A., and Kiwi-Minsker, L. (2007). "Structured catalyst of Pd/ZnO on sintered metal fibers for 2-methyl-3-butyn-2-ol selective hydrogenation." *Journal of Catalysis*, 251, 213-222.
- [47] Stankiewicz, A.I., Kapteijn, F., and Moulijn, J.A. (2004). "Re-engineering the chemical processing plant". Marcel Dekker Inc. Chapter 6: Structured Catalysts and Reactors: A contribution to process intensification.
- [48] Dautzenberg, F.M., Naber, J. E., and van Ginneken, A.J.J. (1971). Shell's flue gas

- desulfurization process. *Chemical Engineering Progress*, 67, 86-91.
- [49] Gelbein, A. and Buchholz, M. (1991). "Process and Structure for Effecting Catalytic Reaction in Distillation Structure". US Patent 5,073,236.
- [50] de la Iglesia, O., Sebastian, V., Mallada, R., Nikolaidis, G., Coronas, J., Kolb, G., Zapf, R., Hessel, V., and Santamaria, J. (2007). "Preparation of Pt/ZSM-5 films on stainless steel microreactors." *Catalysis Today*, 125(1-2), 2-10.
- [51] Kiwi-Minsker, L., and Renken, A. (2005). "Microstructured reactors for catalytic reactions." *Catalysis Today*, 110(1-2), 2-14.
- [52] Kolb, G., and Hessel, V. (2004). "Micro-structured reactors for gas phase reactions." *Chemical Engineering Journal*, 98(1-2), 1-38.
- [53] Kiwi-Minsker, L., Wolfrath, O., and Renken, A. (2002). "Membrane reactor microstructured by filamentous catalyst." *Chemical Engineering Science*, 57(22-23), 4947-4953.
- [54] Wolfrath, O., Kiwi-Minsker, L., and Renken, A. (2001). "Novel membrane reactor with filamentous catalytic bed for propane dehydrogenation." *Industrial & Engineering Chemistry Research*, 40(23), 5234-5239.
- [55] Horny, C., Kiwi-Minsker, L., and Renken, A. (2004). "Micro-structured string-reactor for autothermal production of hydrogen." 101, 3-9.
- [56] Koptug, I. V., Kovtunov, K. V., Gerkema, E., Kiwi-Minsker, L., and Sagdeev, R. Z. (2007). "NMR microimaging of fluid flow in model string-type reactors." *Chemical Engineering Science*, 62(16), 4459-4468.
- [57] Fei, W., Kuiry, S. C., and Seal, S. (2004). "Inhibition of metastable alumina formation on Fe-Cr-Al-Y alloy fibers at high temperature using titania coating." *Oxidation of Metals*, 62(1-2), 29-44.
- [58] Birks, N. M., G.H. and Pettit, F.S. (2006). *Introduction to the High-Temperature Oxidation of Metals*, Cambridge: Cambridge University Press.
- [59] El Kadiri, H., Molins, R., Bienvenu, Y., and Horstemeyer, M. F. (2005). "Abnormal high growth rates of metastable aluminas on FeCrAl alloys." *Oxidation of Metals*, 64(1-2), 63-97.
- [60] Pint, B. A., Martin, J. R., and Hobbs, L. W. (1995). "The oxidation mechanism of theta-Al₂O₃ scales." *Solid State Ionics*, 78(1-2), 99-107.
- [61] Berthome, G., N'Dah, E., Wouters, Y., and Galerie, A. (2005). "Temperature dependence of metastable alumina formation during thermal oxidation of FeCrAl foils." *Materials and Corrosion-Werkstoffe Und Korrosion*, 56(6), 389-392.
- [62] Komhom, S., Mekasuwandumrong, O., Praserthdam, P., and Panpranot, J. (2008). "Improvement of Pd/Al₂O₃ catalyst performance in selective acetylene hydrogenation using mixed phases Al₂O₃ support." *Catalysis Communications*, 10(1), 86-91.
- [63] Ozawa, M., and Kimura, M. (1990). "Effect of cerium addition on the thermal-stability of gamma-alumina support." *Journal of Materials Science Letters*, 9(3), 291-293.
- [64] G. Ertl, H. K., J. Weitkamp. (1999). "Preparation of Solid Catalysts". City: WILEY-VCH Verlag GmbH: Weinheim.
- [65] Trueba, M., and Trasatti, S. P. (2005). "Gamma-alumina as a support for catalysts: A review of fundamental aspects." *European Journal of Inorganic Chemistry*(17), 3393-3403.
- [66] Stott, F. H., Wood, G. C., and Stringer, J. (1995). "The influence of alloying elements on the development and maintenance of protective scales." *Oxidation of Metals*, 44(1), 113-

- 145.
- [67] Pint, B., Treska, M., and Hobbs, L. (1997). "The effect of various oxide dispersions on the phase composition and morphology of Al₂O₃ scales grown on β-NiAl." *Oxidation of Metals*, 47(1), 1-20.
- [68] Zhou, R. S., and Snyder, R. L. (1991). "Structures and transformation mechanisms of the Eta, Gamma and Theta transition aluminas." *Acta Crystallographica Section B-Structural Science*, 47, 617-630.
- [69] Brumm, M. W., and Grabke, H. J. (1992). "The oxidation behavior of NiAl. 1. Phase transformations in the alumina scale during oxidation of NiAl and NiAl-Cr alloys." *Corrosion Science*, 33(11), 1677-1690.
- [70] Whittle, D. P., and Stringer, J. (1980). "Improvements in high temperature oxidation resistance by additions of reactive elements or oxide dispersions." *Philosophical Transactions of the Royal Society of London Series a-Mathematical Physical and Engineering Sciences*, 295(1413), 309-329.
- [71] Tien, J. K., and Pettit, F. S. (1972). "Mechanism of oxide adherence on Fe-25Cr-4Al (Yor Sc) alloys." *Metallurgical Transactions*, 3(6), 1587-1590.
- [72] Vanmanen, P. A., Young, E. W. A., Schalkoord, D., Vanderwekken, C. J., and Dewit, J. H. W. (1988). "The influence of Y on the structure and growth mechanism of alumina scales." *Surface and Interface Analysis*, 12(1-12), 391-396.
- [73] Ramanarayanan, T. A., Ayer, R., Petkovicluton, R., and Leta, D. P. (1988). "The influence of Yttrium on oxide scale growth and adherence." *Oxidation of Metals*, 29(5-6), 445-472.
- [74] Moon, D. P. (1989). "Role of reactive elements in alloy protection." *Materials Science and Technology*, 5(8), 754-764.
- [75] Cueff, R., Buscail, H., Caudron, E., Riffard, F., Issartel, C., and El Messki, S. (2004). "Effect of reactive element oxide coating on the high temperature oxidation behaviour of FeCrAl alloys." *Applied Surface Science*, 229(1-4), 233-241.
- [76] Burtin, P., Brunelle, J. P., Pijolat, M., and Soustelle, M. (1987). "Influence of surface area and additives on the thermal stability of transition alumina catalyst supports. 1. Kinetic data." *Applied Catalysis*, 34(1-2), 225-238.
- [77] Ozawa, M., Kimura, M., and Isogai, A. (1990). "Thermal stability and characterization of γ-Al₂O₃ modified with rare earths." *Journal of the Less-Common Metals*, 162(2), 297-308.
- [78] Cassie, A. B. D., and Baxter, S. (1944). "Wettability of porous surfaces." *Transactions of the Faraday Society*, 40, 0546-0550.
- [79] Wenzel, R. N. (1936). "Resistance of solid surfaces to wetting by water." *Industrial and Engineering Chemistry*, 28, 988-994.
- [80] Patankar, N. A. (2003). "On the modeling of hydrophobic contact angles on rough surfaces." *Langmuir*, 19(4), 1249-1253.
- [81] Zheng, Q. S., Yu, Y., and Zhao, Z. H. (2005). "Effects of hydraulic pressure on the stability and transition of wetting modes of superhydrophobic surfaces." *Langmuir*, 21(26), 12207-12212.
- [82] Nychka, J. A., and Clarke, D. R. (2005). "Quantification of Aluminum Outward Diffusion During Oxidation of FeCrAl Alloys." *Oxidation of Metals*. 63, 325-352.
- [83] Gentleman, M. M., and Ruud, J. A. (2009). "Role of Hydroxyls in Oxide Wettability." *Langmuir*, 26(3), 1408-1411.

- [84] Blonski, S., and Garofalini, S. H. (1993). "Molecular dynamics simulations of [alpha]-alumina and [gamma]-alumina surfaces." *Surface Science*, 295(1-2), 263-274.
- [85] Gerald L. Vaneman, D. R. S. (1990). "Accelerated whisker growth on iron-chromium-aluminum alloy foil ". City: General Motors Corporation, Detroit, Michigan, US
- [86] Nijhuis, T. A.; van Koten, G.; Kapteijn, F.; Moulijn, J. A. Separation of Kinetics and Mass-Transport Effects for a Fast Reaction: the Selective Hydrogenation of Functionalized Alkynes. *Catal. Today* **2003**, 79-80, 315.
- [87] Bruhwiler, A., Semagina, N., Grasmann, M., Renken, A., Kiwi-Minsker, L., Saaler, A., Lehmann, H., Bonrath, W., and Roessler, F. (2008). "Three-Phase Catalytic Hydrogenation of a Functionalized Alkyne: Mass Transfer and Kinetic Studies with in Situ Hydrogen Monitoring." *Industrial & Engineering Chemistry Research*, 47(18), 6862-6869.
- [88] Ma, R., and Semagina, N. (2010). "Nanoparticle shape effect study as efficient tool to reveal structure sensitivity of olefinic alcohol hydrogenation". *The Journal of Physical Chemistry C*. In print. DOI: 10.1021/jp103754b.
- [89] Assael, M. J., and Polimatidou, S. K. (1994). "Measurements of the viscosity of alcohols in the temperature range 290–340 K at pressures up to 30 MPa." *International Journal of Thermophysics*, 15(1), 95-107.
- [90] Vannice, M. A. (2005). *Kinetics of Catalytic Reactions* New York: Springer.
- [91] Leviness, S., Nair, V., Weiss, A. H., Schay, Z., and Gucci, L. (1984). "Acetylene hydrogenation selectivity control on PdCu/Al₂O₃ catalysts." *Journal of Molecular Catalysis*, 25(1-3), 131-140.
- [92] Bates, R. L., Fondy, P. L., and Corpstein, R. R. (1963). "Examination of Some Geometric Parameters of Impeller Power." *Industrial & Engineering Chemistry Process Design and Development*, 2(4), 310-314.
- [93] Sano Y.; Yamaguchi, N. A., T. (1974). "Mass Transfer coefficients for suspended Particles in Agitated Vessels and Bubble columns." *Journal of Chemical Engineering of Japan*, 7, 255-261.
- [94] Nychka J.A. and Samad, J. E. (2010). "Wettability of thermally grown aluminum oxide : Mimicking the lotus leaf". US Provisional Patent. S/N : 61/304,137. Edmonton, Canada.
- [95] Fujikawa, S., and Akamatsu, T. (1980) "Effects of non-equilibrium condensation of vapour on the pressure wave produced by the collapse of a bubble in a liquid". *J. Fluid Mech.*, 97(3), 481-512.
- [96] Valentini, M., Groppi, G., Cristiani, C., Levi, M., Tronconi, E. and Forzatti, P. (2001). "The deposition of gamma- Al₂O₃ layers on ceramic and metallic supports for the preparation of structured catalysts." *Catalysis. Today*. 69, 307.